



저작자표시-비영리-변경금지 2.0 대한민국

이용자는 아래의 조건을 따르는 경우에 한하여 자유롭게

- 이 저작물을 복제, 배포, 전송, 전시, 공연 및 방송할 수 있습니다.

다음과 같은 조건을 따라야 합니다:



저작자표시. 귀하는 원저작자를 표시하여야 합니다.



비영리. 귀하는 이 저작물을 영리 목적으로 이용할 수 없습니다.



변경금지. 귀하는 이 저작물을 개작, 변형 또는 가공할 수 없습니다.

- 귀하는, 이 저작물의 재이용이나 배포의 경우, 이 저작물에 적용된 이용허락조건을 명확하게 나타내어야 합니다.
- 저작권자로부터 별도의 허가를 받으면 이러한 조건들은 적용되지 않습니다.

저작권법에 따른 이용자의 권리는 위의 내용에 의하여 영향을 받지 않습니다.

이것은 [이용허락규약\(Legal Code\)](#)을 이해하기 쉽게 요약한 것입니다.

[Disclaimer](#)

Thesis for the Degree of Master of Engineering

**Synthesis of magnetic hydroxyapatite and
magnetic core-shell nanoparticles for biomedical
applications**



By

Rajarathinam Thenmozhi

Department of Biomedical Engineering

The Graduate School

Pukyong National University

February 2019

Synthesis of magnetic hydroxyapatite and magnetic core-shell nanoparticles for biomedical applications

(생물 의학적 응용을 위한 자기 수산화 인회석 및 자기 코어 껍질 나노 입자의 합성)

Advisor: Junghwan Oh

by

Rajarathinam Thenmozhi



A thesis submitted in partial fulfillment of the requirements for the degree of

Master of Engineering

In Department of Biomedical Engineering

The Graduate School

Pukyong National University

February 2019

Synthesis of magnetic hydroxyapatite and magnetic core-shell nanoparticles for biomedical applications

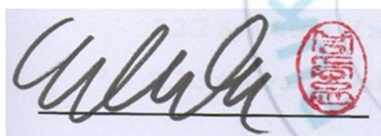
(생물 의학적 응용을 위한 자기 수산화 인회석 및 자기 코어 껍질 나노 입자의 합성)

A dissertation

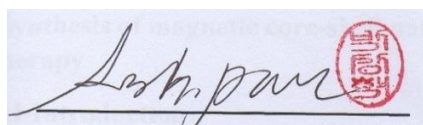
By

Rajarathinam Thenmozhi

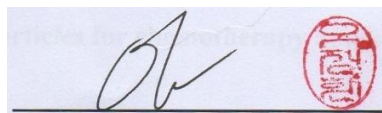
Approved by:



Chairman: Seung Yun Nam



Member: Park Sang Hyug



Member: Junghwan Oh

February 2019

CONTENTS

Table of contents	i
Abstract	iii
List of Schemes	iv
List of Figures	iv
Chapter 1 Introduction	1
1.1. Background	1
1.2. Aim of the Study	4
Chapter 2	
Synthesis and characterization of magnetic hydroxyapatite	5
2.1 Introduction	5
2.2 Materials and Methods	7
2.2.1 Materials	7
2.2.2 Synthesis of magnetic hydroxyapatite	9
2.2.3 Characterization of magnetic hydroxyapatite	10
2.3 Results and Discussion	11
2.4 Conclusion	20
Chapter 3	
Synthesis of magnetic core-shell nanoparticles for chemotherapy applications in cancer therapy	22
3.1 Introduction	22
3.2 Materials and Methods	24
3.2.1 Materials	24
3.2.2 Synthesis of magnetic core-shell nanoparticles	25
3.2.3 Characterization of magnetic core-shell nanoparticles	26
3.3 Results and Discussion	28

3.4 Conclusion	41
Chapter 4	
Conclusions	42
References	43
Acknowledgements	45



Department of Biomedical Engineering,
The Graduate School, Pukyong National University

Abstract

We have prepared a core-shell magnetic@silica-based hydroxyapatite, $\text{Fe}_3\text{O}_4@\text{SiO}_2@\text{HAp}$ composite materials for pH-responsive drug delivery applications. A hydrophilic drug, captopril (Cap) and hydrophobic drug, ibuprofen (Ibu) was chosen as a model hydrophilic and hydrophobic drugs. The drugs was encapsulated into the $\text{Fe}_3\text{O}_4@\text{SiO}_2@\text{HAp}$ composite via electrostatic interactions with existed amine and carboxylic acid groups during calcium phosphate (CaP) shell formation.. We have tested the release behavior of Cap and Ibu drugs under different pH conditions such as neutral pH (pH 7.4) and acidic pH (pH 5.0), respectively. The study result reveal that the synthesized $\text{Fe}_3\text{O}_4@\text{SiO}_2@\text{HAp}$ composite is suitable for release of both water soluble and water non-soluble drugs based on a pH-responsive controlled manner. The study on the straightforward fabrication of polyethylenimine-doxorubicin (PEI-DOX) $\text{Fe}_3\text{O}_4@\text{SiO}_2@\text{TiO}_2$ core-shell nanoparticles for pH stimuli-responsive drug delivery applications. The fabricated nanocarrier system consists of a magnetic iron core (Fe_3O_4), silica shell (SiO_2), titania second shell (TiO_2) and the final PEI cationic polymer shell with an drug DOX for pH-responsive drug delivery applications. We have observed the release behavior of the drug DOX under different pH conditions. The study results reinforce that the synthesized PEI-DOX $\text{Fe}_3\text{O}_4@\text{SiO}_2@\text{TiO}_2$ core-shell nanoparticles are suitable for pH stimuli responsive drug release system. In addition to their excellent drug release performance, the system demonstrates good efficacy against the MDA-MB-231 breast cancer cells. Therefore, the fabricated $\text{Fe}_3\text{O}_4@\text{SiO}_2@\text{TiO}_2$ core-shell nanoparticles act as a good nanodrug carrier for loading and releasing DOX.

Keywords: Iron oxide, Silica coating, Hydroxyapatite, Titania, Core-shell nanoparticles, drug delivery.

LIST OF SCHEMES

Scheme 1. Schematic representation for the Surface chemical modification onto the $\text{Fe}_3\text{O}_4@\text{SiO}_2$ nanoparticles to produce high content of carboxylic acid groups.....	8
Scheme 2. Schematic representation for the formation of hydroxyapatite shell on to the $\text{Fe}_3\text{O}_4@\text{SiO}_2$ nanoparticles to obtain $\text{Fe}_3\text{O}_4@\text{SiO}_2@\text{HAp}$ composite materials....	10
Scheme 3. Schematic illustration of the design of PEI-DOX@ $\text{Fe}_3\text{O}_4@\text{SiO}_2@\text{TiO}_2$ core-shell nanoparticles for drug release under pH stimuli in cancer therapy.....	24

LIST OF FIGURES

Fig. 1 Wide-angle XRD patterns of (a) pristine Fe_3O_4 nanoparticles and (b) $\text{Fe}_3\text{O}_4@\text{SiO}_2@\text{HAp}$ composite materials	12
Fig. 2 TEM images of (a, b) $\text{Fe}_3\text{O}_4@\text{SiO}_2$ particles and (c, d) $\text{Fe}_3\text{O}_4@\text{SiO}_2@\text{HAp}$ composite materials.	13
Fig. 3 Energy dispersive X-ray diffraction (EDX) spectra of (a) $\text{Fe}_3\text{O}_4@\text{SiO}_2$ particles and (b) $\text{Fe}_3\text{O}_4@\text{SiO}_2@\text{HAp}$ composite materials.	14
Fig. 4 SEM images of (a) $\text{Fe}_3\text{O}_4@\text{SiO}_2$ particles and (b) $\text{Fe}_3\text{O}_4@\text{SiO}_2@\text{HAp}$ composite materials.	15
Fig. 5 Particle size distributions (DLS) of (a) $\text{Fe}_3\text{O}_4@\text{SiO}_2$ particles and (b) $\text{Fe}_3\text{O}_4@\text{SiO}_2@\text{HAp}$ composite materials.....	15
Fig. 6 FTIR analysis of (a) Fe_3O_4 nanoparticles (b) $\text{Fe}_3\text{O}_4@\text{SiO}_2@\text{APTES}@\text{COOH}$ particles and (c) $\text{Fe}_3\text{O}_4@\text{SiO}_2@\text{HAp}$ composite materials.....	17

Fig. 7 TGA profile curves of (a) $\text{Fe}_3\text{O}_4@\text{SiO}_2$ nanoparticles and (b) $\text{Fe}_3\text{O}_4@\text{SiO}_2@\text{HAp}$ composites.....	18
Fig. 8 <i>In vitro</i> drug release profiles of (a) Cap and (b) IBU drugs at different pH conditions (pH 7.4 and 5.5, respectively) in PBS buffer medium.....	20
Fig. 9 Wide-angle XRD patterns of (a) pristine Fe_3O_4 nanoparticles, (b) $\text{Fe}_3\text{O}_4@\text{SiO}_2$ (c) $\text{Fe}_3\text{O}_4@\text{SiO}_2@\text{TiO}_2$ (d) PEI $\text{Fe}_3\text{O}_4@\text{SiO}_2@\text{TiO}_2$ core-shell nanoparticles.....	29
Fig. 10 FTIR analysis of (a) Fe_3O_4 nanoparticles (b) $\text{Fe}_3\text{O}_4@\text{SiO}_2$ (c) $\text{Fe}_3\text{O}_4@\text{SiO}_2@\text{TiO}_2$ and (d) PEI-DOX $\text{Fe}_3\text{O}_4@\text{SiO}_2@\text{TiO}_2$ core-shell nanoparticles....	31
Fig. 11 TGA profile curves of (a) $\text{Fe}_3\text{O}_4@\text{SiO}_2$ (b) $\text{Fe}_3\text{O}_4@\text{SiO}_2@\text{TiO}_2$ core-shell (c) PEI $\text{Fe}_3\text{O}_4@\text{SiO}_2@\text{TiO}_2$ core-shell nanoparticles without DOX loading.....	32
Fig. 12 SEM images of (a) Fe_3O_4 nanoparticles (b) $\text{Fe}_3\text{O}_4@\text{SiO}_2$ nanoparticles and (c) $\text{Fe}_3\text{O}_4@\text{SiO}_2@\text{TiO}_2$ core-shell nanoparticles.....	33
Fig. 13 TEM images of the (a) Fe_3O_4 nanoparticles (b) $\text{Fe}_3\text{O}_4@\text{SiO}_2$ (c) $\text{Fe}_3\text{O}_4@\text{SiO}_2@\text{TiO}_2$ nanoparticles and the inset is the TEM of a single particle.....	34
Fig. 14 EDX analysis of (a) $\text{Fe}_3\text{O}_4@\text{SiO}_2$ nanoparticles and (b) $\text{Fe}_3\text{O}_4@\text{SiO}_2@\text{TiO}_2$ core-shell nanoparticles.....	35
Fig. 15 Particle size distributions (DLS) of (A) PEI@ $\text{Fe}_3\text{O}_4@\text{SiO}_2@\text{TiO}_2$ core-shell nanoparticles and (B) Zeta potential of the PEI@ $\text{Fe}_3\text{O}_4@\text{SiO}_2@\text{TiO}_2$ core-shell nanoparticles.....	36
Fig. 16 <i>In vitro</i> drug release profiles of (a) DOX drug at different pH conditions (pH 7.2, pH 5.4 and 4.0, respectively) in PBS buffer medium.....	38
Fig. 17 MTT assay of cells treated with $\text{Fe}_3\text{O}_4@\text{SiO}_2@\text{TiO}_2$ and	

PEI-DOX Fe₃O₄@SiO₂@TiO₂ particles at various concentration.40

Fig. 18 Trypan blue cell viability of MDA MB-231 cells incubated (a) without nanoparticles as Control (b) Fe₃O₄@SiO₂@TiO₂ treated cells with the fixed concentration 80 µg/mL and (c) 20 µg/mL PEI Fe₃O₄@SiO₂@TiO₂ DOX treated cells respectively.....41



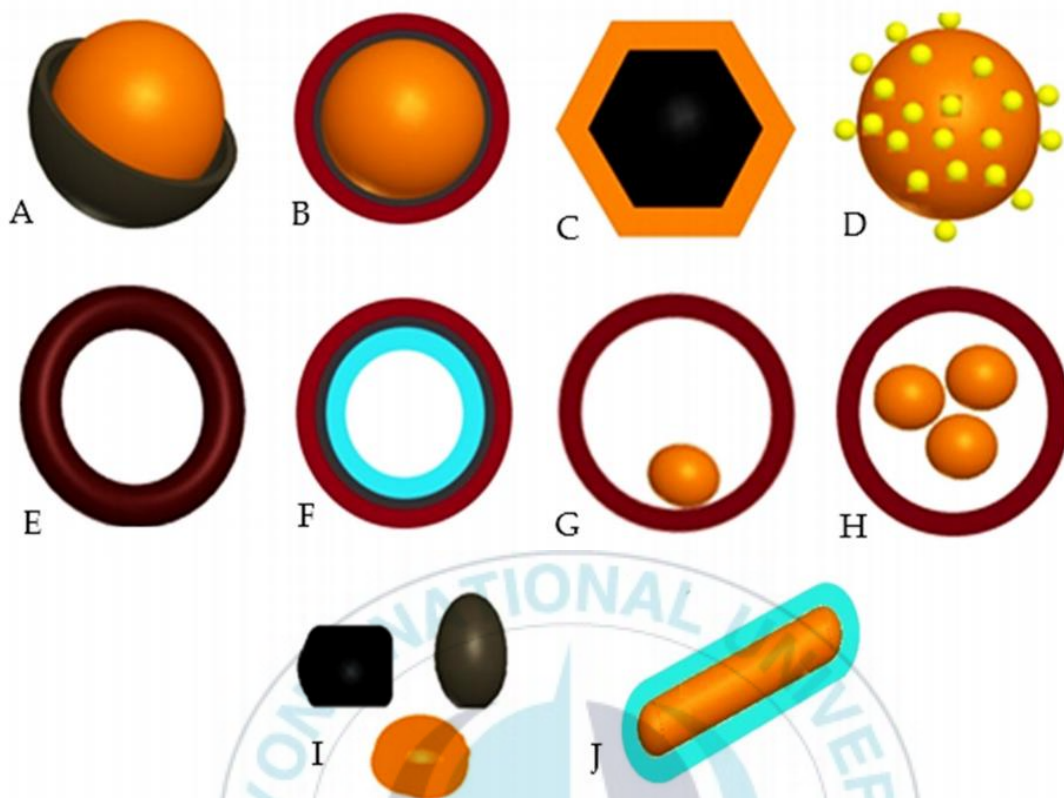
Chapter 1

Introduction

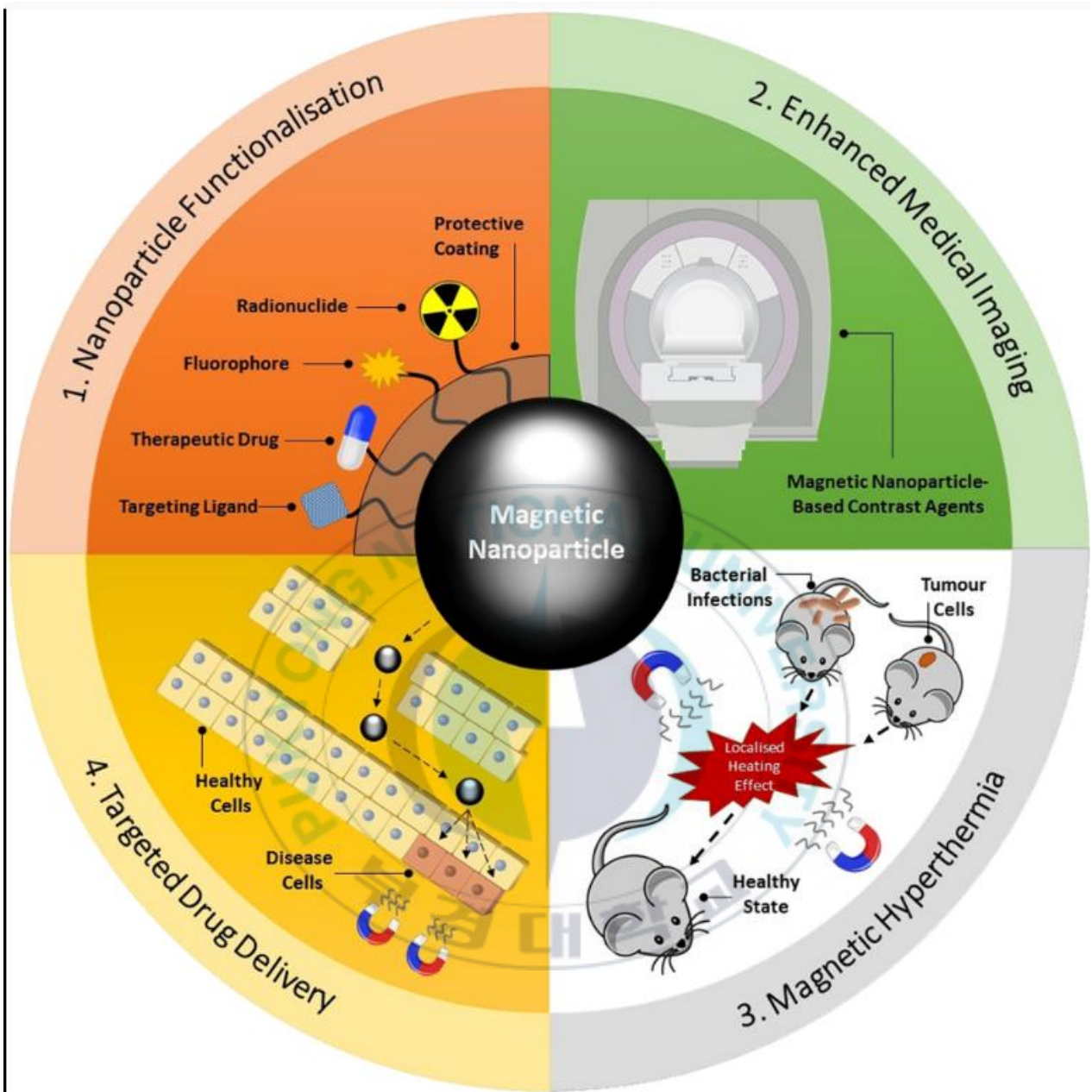
1.1 Background

Nanoparticles have found wide spread application in varied fields of engineering. Nanomaterials are having one or more dimension in the range of nanometer scale and show novel properties from the bulk materials. The nanoparticles are always at the centre of attraction and are categorized as simple and core/shell or composite nanoparticles. The core/shell type nanoparticles can be broadly defined as a core (inner material) and a shell (outer layer material) of different materials in close interaction, including inorganic/inorganic, inorganic/organic, organic/inorganic, organic/organic, combinations. The multiple core core/shell particles are formed when a single shell material is coated on many small core particles together.

Recently, core-shell nanostructures have been found to have improved properties and potential applications have been identified in the field of biomedical engineering.



Schematic (A-J) pictures of different structure of core-shell nanoparticles: (A) Core shell nanoparticles; (B) Core double shell particles or core multi-shell nanoparticle; (C) Polyhedral core/shell nanoparticles; (D) Core porous-shell nanoparticles; (E) Hollow-core shell nanoparticles or single-shell nanoparticles; (F) Hollow-core double-shell nanoparticles; (G) Moveable-core-shell nanoparticles; (H) Multi-core shell nanoparticles; (I) Irregular shape core shell nanoparticles; and, (J) Rod core shell nanoparticles. [1].



Functionalization and therapeutic applications of magnetic nanoparticles. [2].

1.2 Aim of the study

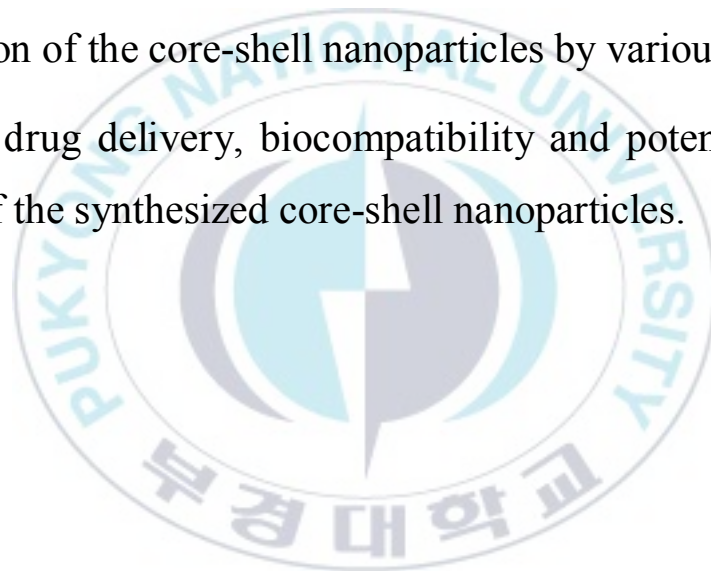
The aim of the present study is to investigate the methods of preparation of magnetic hydroxyapatite and magnetic core-shell nanoparticles. The following objectives of work were identified:

Literature review on preparation of core-shell nanoparticles and its modifications.

Synthesis of core-shell nanoparticles with tailored nanostructures.

Characterization of the core-shell nanoparticles by various techniques.

Evaluation of drug delivery, biocompatibility and potential biomedical applications of the synthesized core-shell nanoparticles.



Chapter 2. Synthesis of magnetic hydroxyapatite for drug delivery applications

1. Introduction

The controlled release of active therapeutic agents from an inert matrix has become increasingly important for oral, transferal, and implantable therapeutic systems due to the advantages of safety, efficiency, and patient convenience. Generally, the most of the drug delivery systems are designed based on environmental stimuli-based release of drugs in a desired dosage for therapeutic medications with fewer side effects. Mostly, the pH-responsive drug delivery systems deliver the drugs under acidic pH environment since the intracellular pH is lower than that in normal tissues [3]. For example, the acidic cellular environments, such as in endosomes and lysosomes, are increases the pH-based drug release efficiency [4]. Generally, surface modification approaches are applied for a drug delivery carrier to prevent or to minimize the pre-leakage of the loaded drugs from the drug carrier system in the undesirable sites and to improve the release efficiency of the drug carriers [5, 6].

Mostly, the inorganic substances such as titania, alumina, silica and calcium phosphates are utilized to prepared drug delivery carriers because the inorganic substances are mostly biocompatible, biodegradable and less expensive than the organic substances [7-10]. The hydroxyapatite (HAp), a natural inorganic and biocompatible material, is the most widely accepted biomaterial, which has been used in drug delivery system, artificial body argons, medical implants and artificial blood trachea owing to the excellent biocompatibility, bioactivity and osteoconductivity [11-13]. Nowadays, calcium phosphate has received much attention in biomedical field over the organic and inorganic counterparts [14]. The HAp material can encapsulate drugs or biomolecules and enable to protect them from enzymatic degradation and can effectively deliver them in a target sites [15-17] because the HAp is stable in neutral pH conditions and can readily dissolved in the acidic environment and therefore, the encapsulated drugs can be effectively released in the desired target sites.

Recently, the use of hydroxyapatite shell coating onto the surface modified core nanoparticles with drug containing core phase received considerable attention [18, 19]. Because, these types of core-shell composite materials have been considered as an efficient drug delivery system in biomedical technology for their advancements. Generally, solid metallic core such as iron oxide nanoparticles are widely used as core nanoparticles. In particular, the development of iron oxide nanoparticles exemplifies this advancement owing to its characteristics of non-toxic, biocompatible and biodegradable nature. The magnetic nanoparticles based materials are widely applied in drug delivery applications [20, 21] and other biomedical applications such as magnetic resonance imaging (MRI), biosensing and bioseparation [22-24]. When, using bare iron oxide nanoparticles, it has tendency to aggregate into large clusters and losing their magnetic properties due to its anisotropic dipolar attraction. To overcome this problem, generally, coating of the iron nanoparticles with polymer, biomolecules, silica coating and ligand functionalities are applied [25-27]. Specifically, the coating of silica onto the magnetic nanoparticles surfaces not only stabilize the magnetic iron oxide nanoparticles but it can also be used for further functionalization with other organic functional groups or biocompatible HAp shell. The organic functional groups, specifically, the amine groups and carboxylic acid groups are widely utilized in present research due to its strong nucleophilicity and compatibility. The active amine and carboxylic acid groups are used to conjugate peptides, proteins or antibodies. Also, these functional groups act as chelating ligands owing to the coordination ability with a wide range of metal ions [28].

In this work, we present the preparation of core-shell based $\text{Fe}_3\text{O}_4@\text{SiO}_2@\text{HAp}$ composite materials by solvothermal and chemical group functionalization approach. Firstly, the magnetic Fe_3O_4 nanoparticles are coated with silica by Stöber method. Secondly, the silica surface of the $\text{Fe}_3\text{O}_4@\text{SiO}_2$ particles were immobilized with 3-triethoxysilyl propyl amine (APTES) groups followed by the reaction of the primary amine groups with pyromellitic dianhydride reagent to produce large amount of surface carboxylic acid groups onto the $\text{Fe}_3\text{O}_4@\text{SiO}_2$ particles surfaces. These surface carboxylic acid groups can readily interact with the calcium (Ca^{2+}) ions by metal-ligand coordination process when introducing calcium chloride solution. Finally, the HAp shell

were produced over these calcium coordinated carboxylic acid groups by reacting with ammonium phosphate solution under basic medium to yield $\text{Fe}_3\text{O}_4@\text{SiO}_2@\text{HAp}$ composite material. The synthesized $\text{Fe}_3\text{O}_4@\text{SiO}_2@\text{HAp}$ composite was analyzed by a range of characterizations including X-ray diffraction (XRD), Fourier-transform infrared (FTIR) spectroscopy, scanning and transmission electron (SEM, TEM) microscopic analyses, energy-dispersive X-ray (EDX) spectroscopic analysis and thermogravimetric (TG) analysis. The prepared $\text{Fe}_3\text{O}_4@\text{SiO}_2@\text{HAp}$ composite was used to loading and release of hydrophilic and hydrophobic drugs. For this purpose, we have chosen water soluble captopril (Cap) and water non-soluble ibuprofen (Ibu) as a model drugs and the drug release behavior was evaluated under different pH conditions such as neutral pH (pH 7.4) and acidic pH (pH 5.0) conditions, respectively.

2. Experimental Materials and methods

2.1. Experimental materials

2.1. Reagents

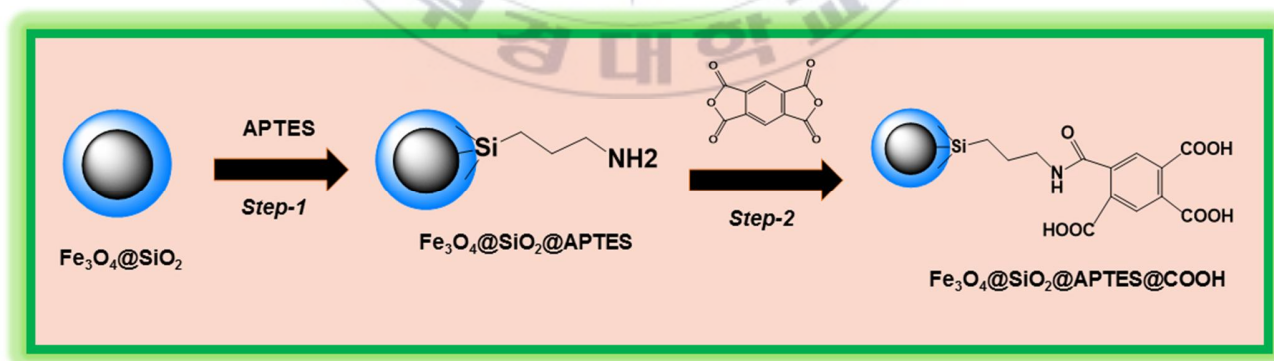
Iron (III) chloride ($\text{FeCl}_3 \cdot 6\text{H}_2\text{O}$), ethylene glycol, sodium acetate, trisodium citrate, 3-(aminopropyl)triethoxy silane (APTES), tetraethyl orthosilicate (TEOS), pyromellitic dianhydride, calcium chloride dehydrate ($\text{CaCl}_2 \cdot 2\text{H}_2\text{O}$), ammonium phosphate dibasic ($(\text{NH}_4)_2\text{HPO}_4$) and sodium hydroxide were purchased from Sigma Aldrich. All the reagents used were of analytical grade and used without further purification.

2.2. Synthesis of iron oxide (Fe_3O_4) nanoparticles

Iron oxide nanoparticles were synthesized by following the previously reported method [29]. About 1 mmol of ferric chloride was dissolved in 15 mL of ethylene glycol and stirred until the solution become clear. To this, 0.9 g of sodium acetate was added and stirred for 2 h followed by the addition of 0.12 g trisodium citrate. The resulted suspension was stirred at room temperature for 4 h. The obtained yellow solution was transferred into Teflon-lined stainless steel autoclave (50 mL capacity) and heated at 200 °C for 8 h. The obtained black product was washed with water and ethanol and then dried at 60 °C.

2.3. Silica coating, APTES and carboxylic acid groups modification onto the Fe_3O_4 nanoparticles

Typically, 0.25 g of Fe_3O_4 nanoparticles was dispersed in 80 mL of ethanol and 20 mL deionized water and sonicated for 10 mins. Next, 0.8 g of TEOS was added dropwise and kept for stirring. To this, about 6 mL of ammonia was added and stirred for another 4 h. The obtained product was collected by external magnet and washed with water and ethanol and then dried at 70 °C. Next, for APTES modifications, about 0.5 g of the silica coated $Fe_3O_4@SiO_2$ sample was dispersed in 60 mL dry toluene. To this, 0.6 mL of APTES was added and stirred at 80 °C for 12 h. Finally, the APTES modified $Fe_3O_4@SiO_2@APTES$ sample was separated and dried at 60 °C. In the next step, the carboxylic acid groups were produced onto the $Fe_3O_4@SiO_2@APTES$ sample by dispersing the $Fe_3O_4@SiO_2@APTES$ nanoparticles in 200 mL ethanol. To this, 0.5 M solution of pyromellitic dianhydride was added and allowed to react at 45 °C, for 12 h. In this step, the amine groups onto the $Fe_3O_4@SiO_2@APTES$ sample was reacted with anhydride part of pyromellitic dianhydride via the formation of –NH–CO– bond and produced reactive carboxylic acid groups [30]. The reacted samples was separated and washed with ethanol and then further hydrolyzed in the presence of acidic condition (0.2 M HCl) to induce ring opening reaction of unreacted parts of pyromellitic groups. Finally, the obtained suspension was separated and dried at 60 °C to obtained $Fe_3O_4@SiO_2@APTES@COOH$ samples.



Scheme 1. Surface chemical modification onto the $Fe_3O_4@SiO_2$ nanoparticles to produce high content of carboxylic acid groups.

2.3. Synthesis of drug loaded and hydroxyapatite shell coated $Fe_3O_4@SiO_2@HAp$ nanoparticles

For hydroxyapatite coating, approximately 0.25 g of $Fe_3O_4@SiO_2@APTES@COOH$ sample was dispersed in 200 mL distilled water. To this, NaOH solution (0.5 mL, 0.1 M) was added to adjust the reaction medium pH to 10. Next, the calcium chloride solution (10 mL, 0.5 M) was added and stirred for 2 h. In this step, the calcium ions (Ca^{2+} ions) were interacted with carboxylic acid groups by coordination complexation of Ca^{2+} ions with COOH groups. In the next step, the ammonium phosphate (20 mL, 1 M) solution was added and allowed to stir for 12 h to grow the hydroxyapatite shell over the $Fe_3O_4@SiO_2@APTES@COOH/Ca^{2+}$ samples. In this step, the pH of the reaction medium was maintained at pH 10. The resulted $Fe_3O_4@SiO_2@HAp$ product precipitate was separated, washed with distilled water and dried at 80 °C, overnight [31].

2.4. The drug loading and *in vitro* drug release

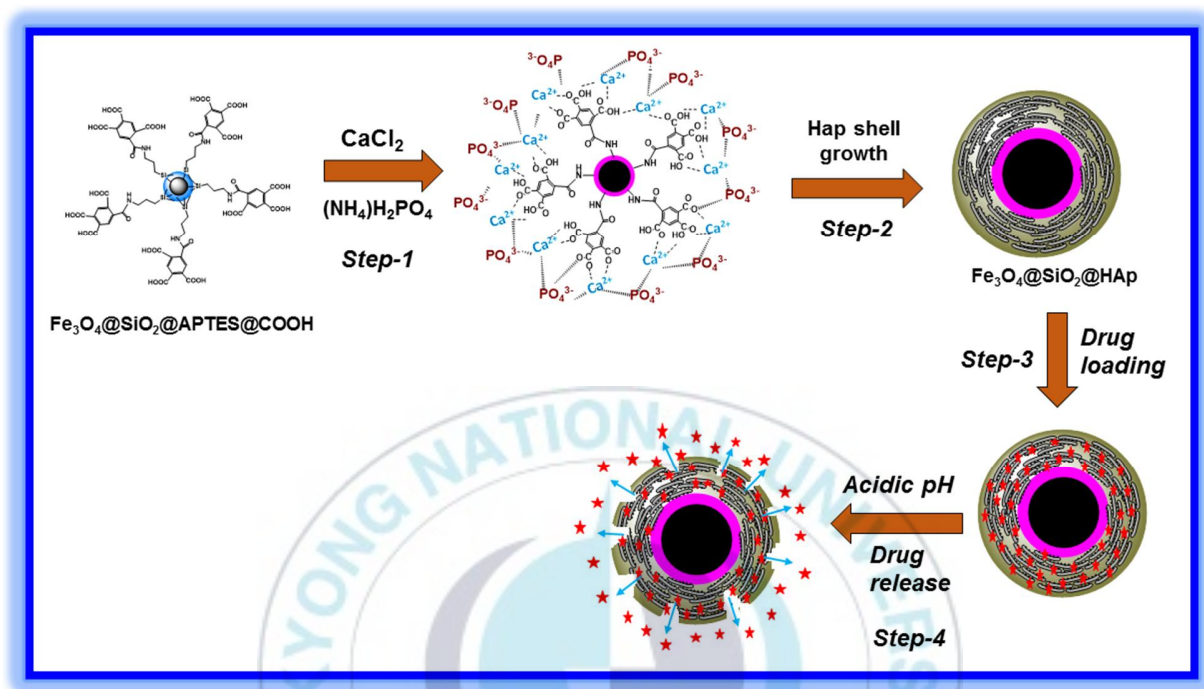
The drugs Cap (10 mg/mL) or Ibu (10 mg/mL) was selected to encapsulate the drug molecules in the amine and carboxyl part of the $Fe_3O_4@SiO_2@APTES@COOH$ samples by diffusion method. After drug loading, the samples were separated, washed and dried at 60 °C. The drug encapsulation efficiency was estimated by the following equation:

$$\text{Encapsulation efficiency (\%)} = \frac{\text{Mass of drug in sample}}{\text{Mass of drug injected}} \times 100$$

From the above equation, the encapsulation efficiency of Cap and Ibu into the $Fe_3O_4@SiO_2@HAp$ composites was estimated to be about 33 % and 42 %, respectively. The considerable drug loading efficiency was achieved due to the presence of large content of drug interacting amine and hydroxyl groups in the modified HAP inorganic shell.

For *in vitro* drug release experiments, about 50 mg of Cap or Ibu drug-loaded $Fe_3O_4@SiO_2@HAp$ nanocomposites was added to 25 ml of PBS buffer and the mixture was shaken at 37 °C in a water bath. The pH of the buffer medium was adjusted to pH 7.4 or pH 5.0, respectively. At different time intervals, 1 ml of aliquots were taken and replaced with 1 ml of fresh solution. The

aliquot was analyzed using UV-visible spectrophotometry at 205 nm for Cap drug or 272 nm for Ibu drug to evaluate the drug release efficiency at different pH conditions.



Scheme 2. Schematic representation for the formation of hydroxyapatite shell onto the Fe₃O₄@SiO₂ nanoparticles to obtain Fe₃O₄@SiO₂@HAp composite materials.

2.5. Characterization

The wide-angle X-ray diffraction (XRD) patterns of the samples was measured using X'Pert-MPD system, Philips, Almelo, Netherlands) X-ray diffractometer with Cu K_α radiation. The synthesized Fe₃O₄@SiO₂@HAp composite materials were characterized using various instruments. The transmission electron microscope (TEM) (JEOL JEM-2100) equipped with an accelerated voltage of 100 kV, with an energy dispersive X-ray spectroscopy (EDX) with an accelerator voltage of 200 kV. The scanning electron microscopy (SEM) images were measured on JEOL GEM 2010) microscope with accelerating voltage of 100 kV. UV-visible absorption spectra were recorded using a Shimadzu UV- 2450 spectrophotometer in a quartz cuvette with a 1 cm path length. Fourier transform infrared (FTIR) spectroscopy was performed with a Perkin-

Elmer Spectrum 100 using KBr pelleting method. Particle size distribution of the sample was measured by dynamic light scattering using Beckman Coulter, LS 13320 particle size analyzer. Thermogravimetric (TG) analysis was done on a TGA 7, Pyris 1, Perkin Elmer thermal analyzer in the temperature range 50 °C to 700 °C with a heating rate 10 °C/min.

3. Results and discussion

Fig. 1 shows the XRD patterns of the synthesized Fe₃O₄ nanoparticles and the hydroxyapatite modified Fe₃O₄@SiO₂@HAp composites. In Fig. 1(a), the Fe₃O₄ nanoparticles shows sharp crystalline peaks at 30.7, 35.9, 43.4, 53.9, 58.4 and 63.2 (2θ) corresponding to the XRD reflection planes of (220), (311), (400), (422), (511) and (440), respectively. The results indicate that the prepared Fe₃O₄ nanoparticles diffraction peaks match with the standard XRD patterns (JCPDS 85-1436). After silica coating and HAp modifications, the Fe₃O₄@SiO₂@HAp composites showed additional crystalline XRD peaks 26.8, 32.5, 33.2, 39.4, 47.6, 49.3, 54.4, respectively, for (002), (211), (112), (310) (222), (213), (004) indicating the formation of crystalline HAp shell onto the Fe₃O₄@SiO₂ nanoparticles. All the crystalline peak intensities for the Fe₃O₄@SiO₂@HAp samples are slight decreased than the pristine Fe₃O₄ nanoparticles due to the formation of silica coating and hydroxyapatite shell formed over the Fe₃O₄ nanoparticles.

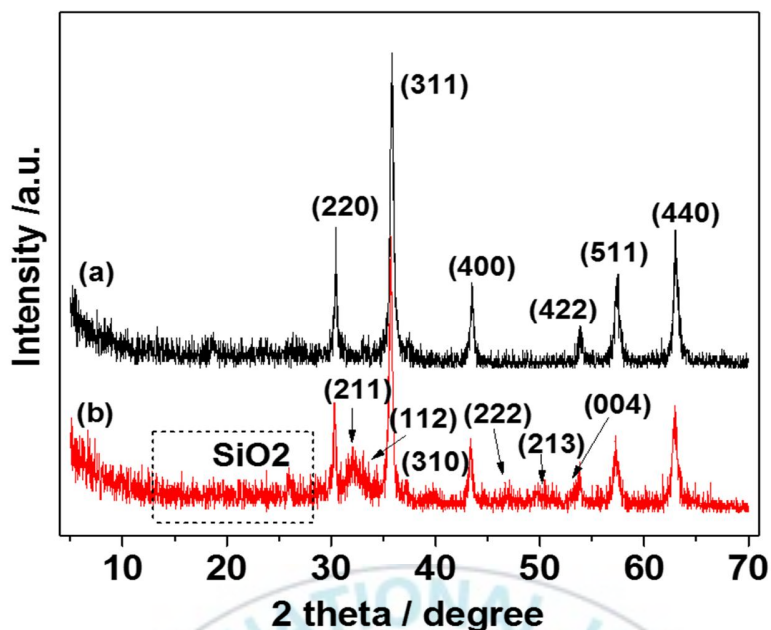


Fig. 1 Wide-angle XRD patterns of (a) pristine Fe_3O_4 nanoparticles and (b) $\text{Fe}_3\text{O}_4@SiO_2@HAp$ composite materials.

The particle shape and surface morphology of the $\text{Fe}_3\text{O}_4@SiO_2@HAp$ nanoparticles were observed by FETEM and FESEM analysis. As shown in Fig. 2, TEM images consists of dark inner part indicating the presence of Fe_3O_4 nanoparticle core and the light contrast middle shell which confirms the formation of silica shell onto the Fe_3O_4 nanoparticle core and the very light contrast outer shell evidencing the formation of crystalline HAp shell formation onto the silica coated Fe_3O_4 nanoparticle. The EDX analysis was used to determine the loading content of elements present in the $\text{Fe}_3\text{O}_4@SiO_2$ nanoparticles are shown in Fig. 3(a). The EDX spectra of the HAp shell modified $\text{Fe}_3\text{O}_4@SiO_2@NH_2@COOH@HAp$ composite particles are shown in Fig. 3(b). From the EDX spectra (Fig. 3(a, b)), the Ca/P molar ratio was estimated to be about $\text{Ca/P} = 1.6$ over the detection region in the CaP shell in the $\text{Fe}_3\text{O}_4@SiO_2@NH_2@COOH@HAp$ particles.

The Ca/P molar ratio estimated from the results suggested that the HAp shell being mineral of calcium phosphate [32]. The calcium phosphate minerals undergo easy soluble under acidic environments and highly responsive to acidic pH conditions.

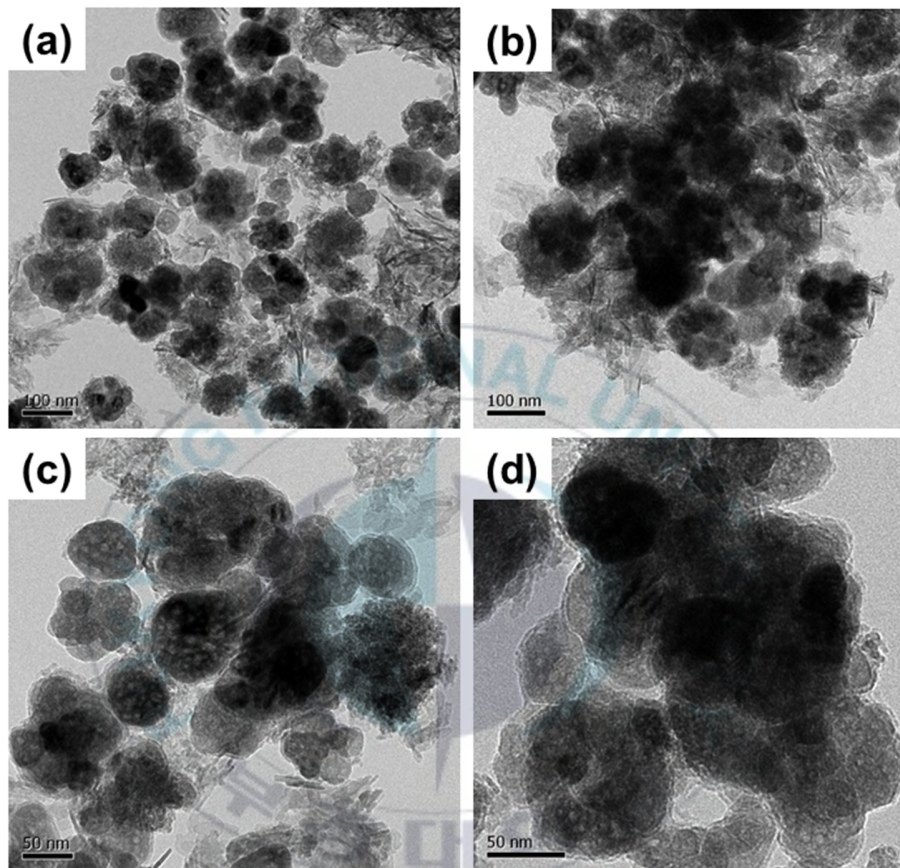


Fig. 2 TEM images of (a, b) $\text{Fe}_3\text{O}_4@SiO_2$ particles and (c, d) $\text{Fe}_3\text{O}_4@SiO_2@HAp$ composite materials.

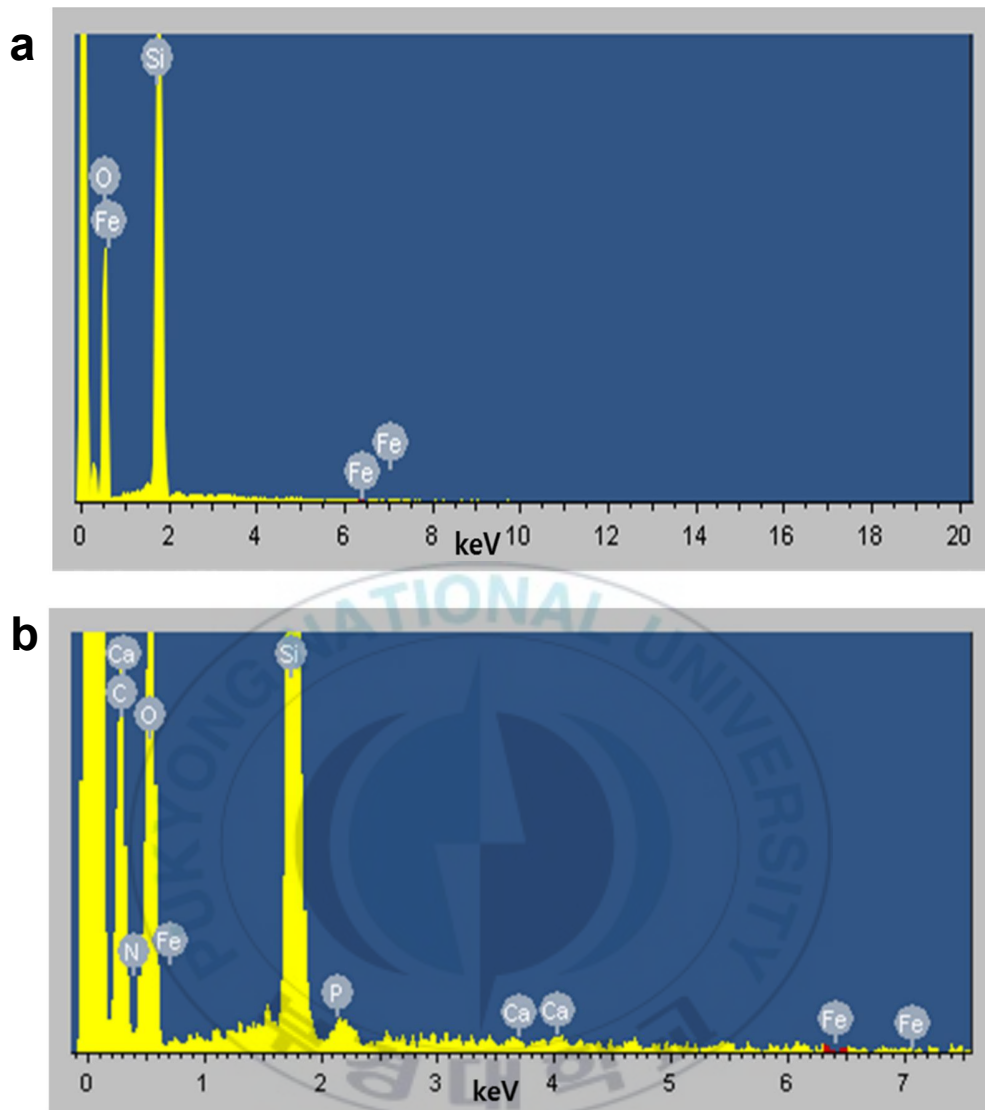


Fig. 3 Energy dispersive X-ray diffraction (EDX) spectra of (a) $\text{Fe}_3\text{O}_4@\text{SiO}_2$ particles and (b) $\text{Fe}_3\text{O}_4@\text{SiO}_2@\text{HAp}$ composite materials.

The surface morphology of the $\text{Fe}_3\text{O}_4@\text{SiO}_2@\text{HAp}$ nanoparticles were also observed by FESEM analysis. As observed in Fig.4, the nanoparticles possess a rough surface with aggregated particles with average particle size about 250-300 nm. The average particle size distribution of the $\text{Fe}_3\text{O}_4@\text{SiO}_2@\text{HAp}$ nanoparticles were also estimated by dynamic light scattering (DLS) measurements (Fig. 5). The average particle size of $\text{Fe}_3\text{O}_4@\text{SiO}_2$ nanoparticles were around 150

nm (Fig. 5 (a)). Furthermore, the average particle size of hydroxyapatite shell modified $\text{Fe}_3\text{O}_4@\text{SiO}_2@\text{HAp}$ composite materials were in the range between 250-300 nm as in Fig. 5 (b). The increased particles size of $\text{Fe}_3\text{O}_4@\text{SiO}_2@\text{HAp}$ composites indicating the formation of HAp shell onto the $\text{Fe}_3\text{O}_4@\text{SiO}_2$ nanoparticles to yield the $\text{Fe}_3\text{O}_4@\text{SiO}_2@\text{HAp}$ composite materials.

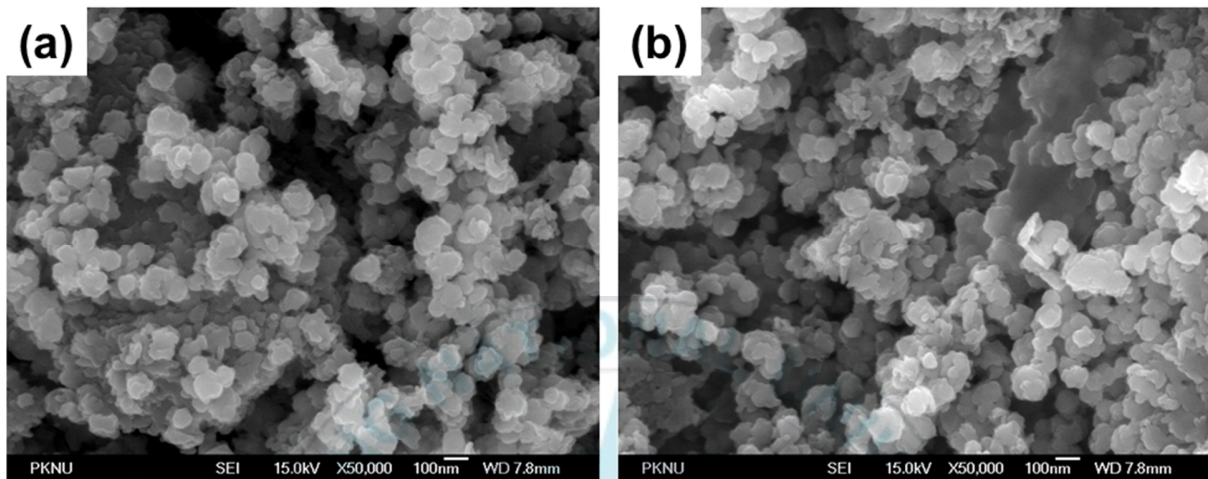


Fig. 4 SEM images of (a) $\text{Fe}_3\text{O}_4@\text{SiO}_2$ particles and (b) $\text{Fe}_3\text{O}_4@\text{SiO}_2@\text{HAp}$ composite materials.

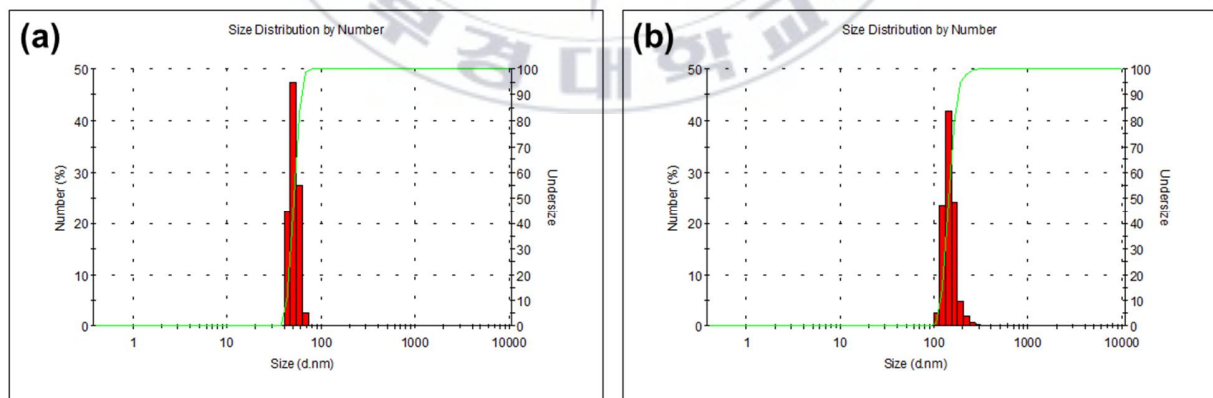


Fig. 5 Particle size distributions (DLS) of (a) $\text{Fe}_3\text{O}_4@\text{SiO}_2$ particles and (b) $\text{Fe}_3\text{O}_4@\text{SiO}_2@\text{HAp}$ composite materials.

The step-wise surface modifications of silica coating, carboxylic acid groups grafting and hydroxyapatite shell coating onto the Fe₃O₄ nanoparticles are characterized by FTIR analysis. Fig. 6, shows all the FTIR spectra have the characteristic stretching peak at 595 cm⁻¹ for Fe-O vibration band indicating the presence of magnetic Fe₃O₄ nanoparticles. After silica coating onto the Fe₃O₄ nanoparticles, the Fe₃O₄@SiO₂ sample shows the vibration peaks at 1098 cm⁻¹ and 957 cm⁻¹ indicating the formation of Si-O-Si network and the presence of surface silanol (Si-OH) groups. The characteristic peaks at 2890 cm⁻¹ and 2918 cm⁻¹ can be assigned to the symmetric and asymmetric C-H groups vibrations of propyl carbon chains (Fig. 6(a)). In addition, the vibration modes at 1405 cm⁻¹, 1625 indicating the presence of amine groups and the hydroxyl groups of carboxylic acid functionalities. In addition, the overlapped peak at 1656 cm⁻¹ indicates the existence of C=O groups in carboxylic acid units (Fig. 6(b)). Furthermore, the formation of hydroxyapatite shell onto the amine modified Fe₃O₄@SiO₂@NH₂@COOH samples, the peak intensity for the C-H stretching has been increased at 2890 cm⁻¹ and 2918 cm⁻¹ (Fig. 6(c)) and the new strong intense peaks are generated at 1686 cm⁻¹ and at 1418 cm⁻¹ indicating the formation of calcium ion coordination with amine groups and the formation of phosphate units present in the inorganic hydroxyapatite shell. The additional broad stretching peak at 3185 cm⁻¹ indicates the presence of carbonate ions. All the characteristic FTIR vibration peaks evidenced for the silica coating, amine, acid grafting and Hap functional shell modifications onto the Fe₃O₄ nanoparticles to yield the Fe₃O₄@SiO₂@HAp nanocomposites were successful. [33].

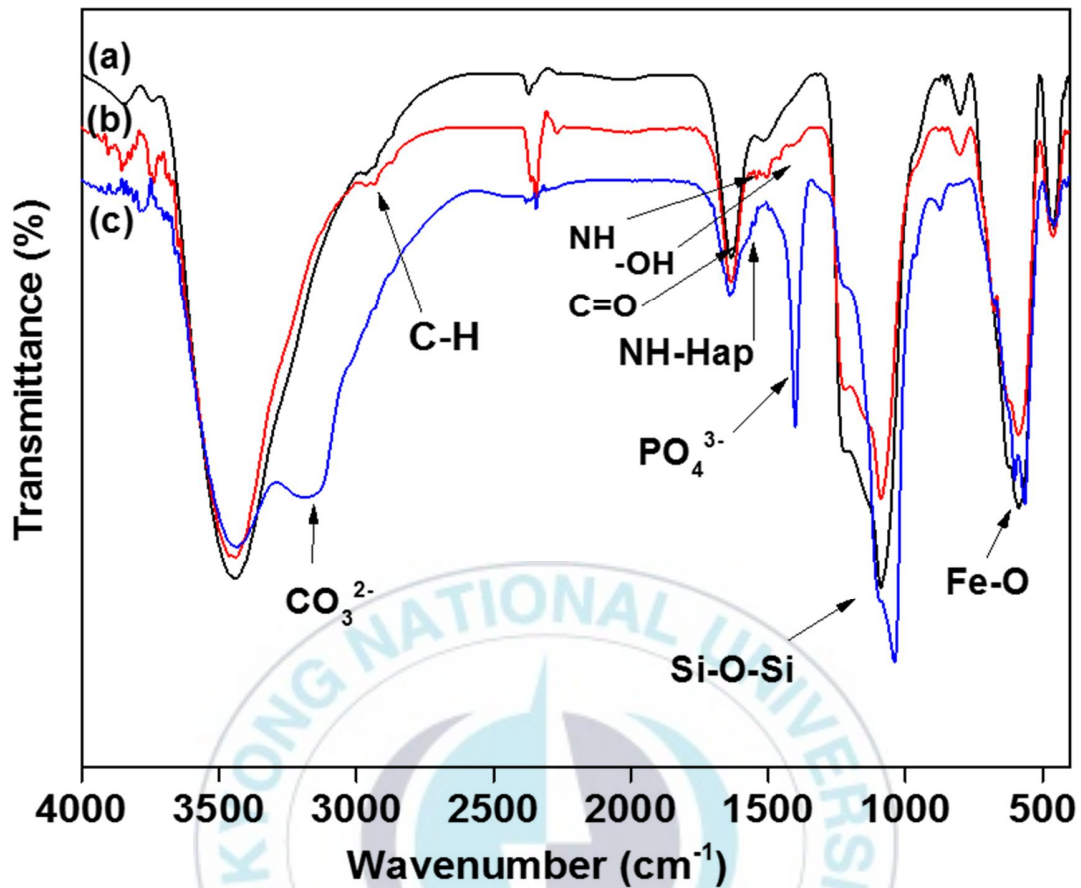


Fig. 6 FTIR analysis of (a) Fe_3O_4 nanoparticles (b) $\text{Fe}_3\text{O}_4@SiO_2@APTES@COOH$ particles and (c) $\text{Fe}_3\text{O}_4@SiO_2@HAp$ composite materials.

The content of modified organic functional groups in the $\text{Fe}_3\text{O}_4@SiO_2@HAp$ nanocomposites was estimated by thermogravimetric (TG) analysis. As shown in Fig.7, both the Fe_3O_4 nanoparticles and $\text{Fe}_3\text{O}_4@SiO_2@HAp$ nanocomposites showed a trace amount of initial weight loss (~ 2.5 wt.%) in the temperature range at 100 °C due to the evaporation of physisorbed water and solvents (Fig. 7(a)). As compared with Fe_3O_4 nanoparticles (Fig. 7(b)), the $\text{Fe}_3\text{O}_4@SiO_2@HAp$ composite had weight loss about ~ 10 wt.% in the temperature range at 101 °C to 650 °C, indicates decomposition of the quantitative amount of surface modified amine and carboxylic acid groups in the $\text{Fe}_3\text{O}_4@SiO_2@HAP$ nanocomposites.

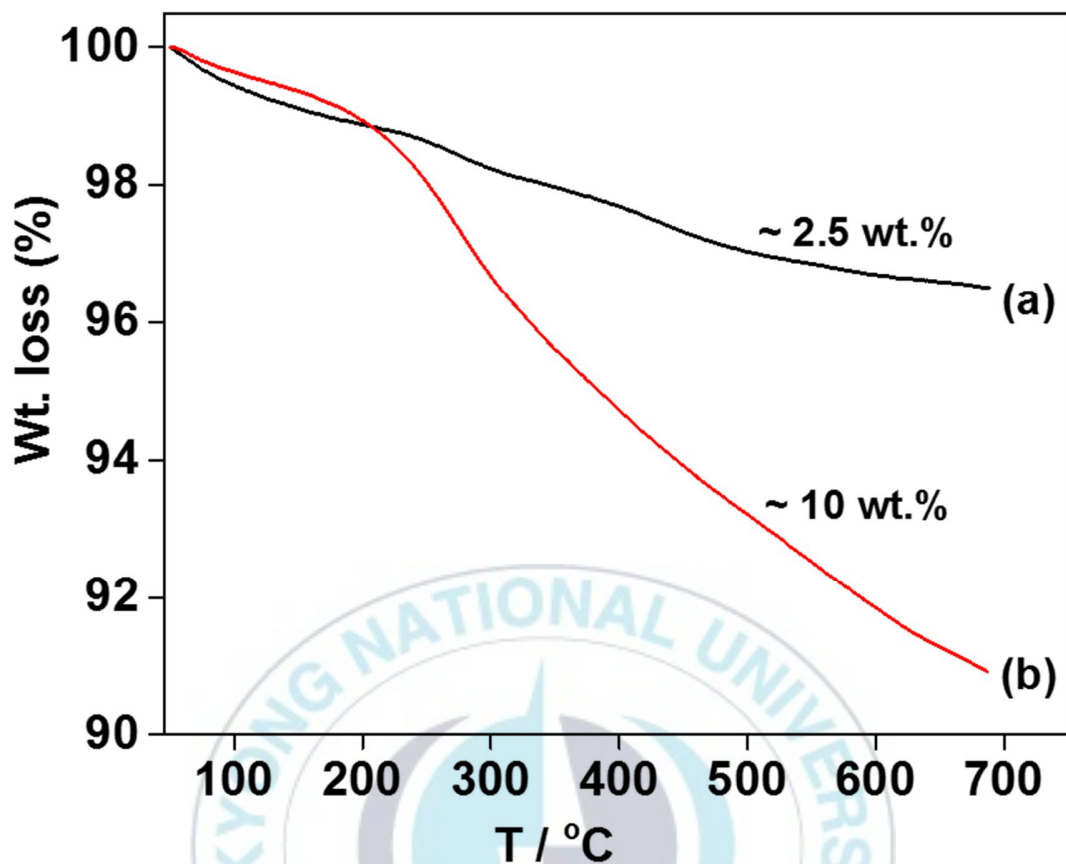


Fig. 7 TGA profile curves of (a) $\text{Fe}_3\text{O}_4@\text{SiO}_2$ nanoparticles and (b) $\text{Fe}_3\text{O}_4@\text{SiO}_2@\text{HAp}$ composites.

To investigate the pH-responsive drug release behavior from $\text{Fe}_3\text{O}_4@\text{SiO}_2@\text{HAp}$ composites, two different pH conditions were employed specifically, pH 7.4 and pH 5.5, respectively. As shown in Fig. 8(a, b), the Cap and Ibu release rate were considerably low about 24 % for Cap and about 19 % of Ibu, respectively, was released at 24 h under physiological pH condition (pH 7.4). In contrary, the Cap and Ibu release rates were enhanced effectively under acidic pH conditions. About, 69 % of Cap and about 81 % of Ibu were released at acidic pH conditions (pH 5.5), respectively, after 24 h. About 24% and 19% of the Cap and Ibu were occurred at pH 7.4 due to the weakly adsorbed and surface adhered drug molecules. On the other hand, the enhanced Cap and Ibu about 69% and 81% was occurred because of the dissolution and dissociation of hydroxyapatite coating under the acidic pH (pH 5.5) condition. Therefore, the impregnated drug molecules with the $\text{Fe}_3\text{O}_4@\text{SiO}_2@\text{HAp}$ composite materials start to dissolve and diffuse out from

the $\text{Fe}_3\text{O}_4@\text{SiO}_2@\text{HAp}$ composites. In addition, the amine and carboxyl groups and the drug molecules were protonated under acidic pH conditions. There is an electrostatic repulsion force is expected between the protonated functional groups and drug molecules and the electrostatic repulsion induce the release of drug molecules from the $\text{Fe}_3\text{O}_4@\text{SiO}_2@\text{HAp}$ composite materials. The overall drug release study results evidenced that the magnetic $\text{Fe}_3\text{O}_4@\text{SiO}_2@\text{HAp}$ composite has potential to be utilized for loading and release of both hydrophilic and hydrophobic drugs based on pH-responsive drug release mechanisms.

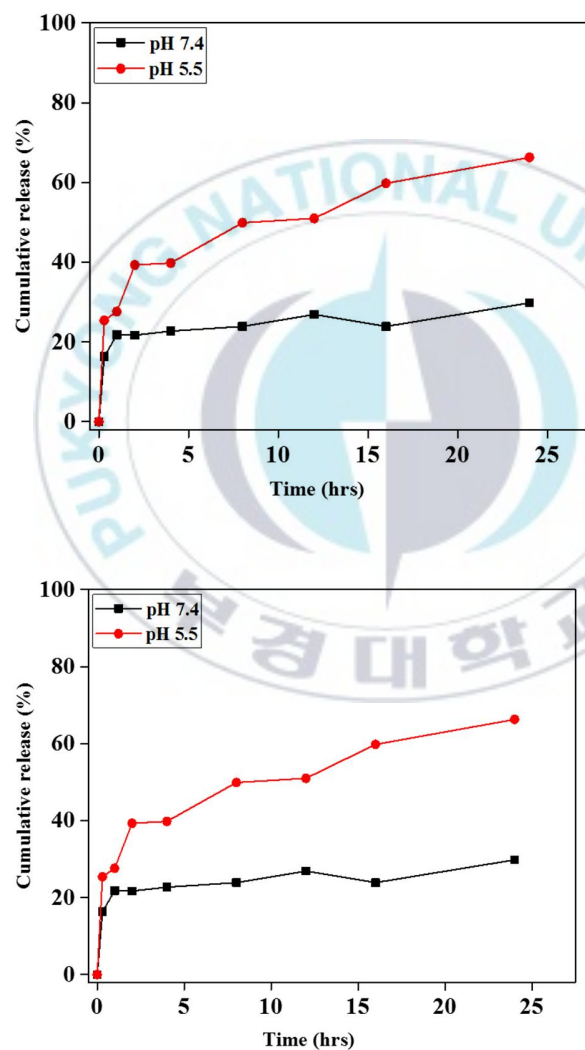


Fig. 8 *In vitro* drug release profiles of (a) Cap and (b) Ibu drugs at different pH conditions (pH 7.4 and 5.5, respectively) in PBS buffer medium.

4. Conclusions

In conclusion, we have synthesized a magnetic hydroxyapatite $\text{Fe}_3\text{O}_4@\text{SiO}_2@\text{HAp}$ composite by solvothermal silica coating and surface chemical modification approaches. The characterizations such as XRD analysis, TEM and FTIR results supports that the silica coating and hydroxyapatite shell formation onto the Fe_3O_4 nanoparticles. From SEM and DLS datas of the prepared $\text{Fe}_3\text{O}_4@\text{SiO}_2@\text{HAp}$ composites show that the sample possesses slightly aggregated particles with rough surface morphology and the average particle size about 250-300 nm. Further, from the TGA data, it was estimated the presence of organic amine and carboxylic acid functional groups present in the $\text{Fe}_3\text{O}_4@\text{SiO}_2@\text{HAp}$ composites was about ~ 10 wt%. In addition, from the EDX spectra, it was calculated that the quantity of Ca/P ratio in the hydroxyapatite shell was determined to be $\text{Ca/P} = 1.6$. The loading capacity of hydrophilic drug, captopril, Cap and hydrophobic drug, Ibu into the $\text{Fe}_3\text{O}_4@\text{SiO}_2@\text{HAp}$ composite were estimated to be about 33 % and 42%, respectively. It was demonstrate that the $\text{Fe}_3\text{O}_4@\text{SiO}_2@\text{HAp}$ composites are capable to release the loaded drugs under acidic pH conditions. About 24 % and about 19 % of Cap and Ibu, respectively, were released at 24 h under physiological pH condition (pH 7.4). On the other hand, the Cap and Ibu release rates were enhanced effectively under acidic pH conditions to about, 69 % and 81 %, respectively after 24 h. Under physiological pH, the hydroxyapatite shells in $\text{Fe}_3\text{O}_4@\text{SiO}_2@\text{HAp}$ composites are more stable and it can inhibit the release of loaded drugs at normal pH conditions. On the other hand, under acidic pH conditions, the Hap shells in $\text{Fe}_3\text{O}_4@\text{SiO}_2@\text{HAp}$ composites undergo dissolution and dissociation and hence the encapsulated drug molecules stated to diffuse out from the $\text{Fe}_3\text{O}_4@\text{SiO}_2@\text{HAp}$ composites. The drug release experimental results reveal that the prepared $\text{Fe}_3\text{O}_4@\text{SiO}_2@\text{HAp}$ composites is a potential drug carrier for delivery of both hydrophilic and hydrophobic drugs in practical applications.

Chapter 3. Synthesis of magnetic core-shell nanoparticles for chemotherapy applications in cancer therapy

1. Introduction

The controlled and targeted drug delivery systems have enticed renewed attention due to the development of a variety of new drug carrier systems as a promising platform for cancer therapeutics. An intelligent anticancer theranostic nanosystem avoids the pitfalls of chemotherapy and drugs encapsulated in the magnetic nanocarriers prevent premature release into the cellular environment, reducing the toxicity towards healthy cells [34, 35]. Various stimuli explored for modulating intelligent drug delivery systems are temperature, light, ultrasonic radiation, magnetic, electric field, pH, ionic strength, redox, enzymes, antibody and inflammation. Among the different types of stimuli, pH has been most widely used to design sensitive nanosystems for drug delivery. The pH sensitive nanocarriers enhance the permeability and retention of drugs in tumors due to the presence of acid-labile chemical bonds that are unstable in acidic pH. This outstanding property makes the pH stimuli-controlled drug delivery as an efficient approach to treat cancers [36-39]. Chemotherapy shrinks the cancer cells and allows the chemotherapeutic drugs to spread throughout the solid tumors in a controlled manner through the enhanced permeability and retention effect (EPR effect) [40-41]. The magnetic nanoparticles are employed for a large panel of dominated biomedical applications such as immunoassays, cell-labelling, targeted drug delivery, magnetic hyperthermia, bioimaging, visible light photocatalysis, photodynamic and photothermal therapy, magnetic separation biosensors etc. [42-44].

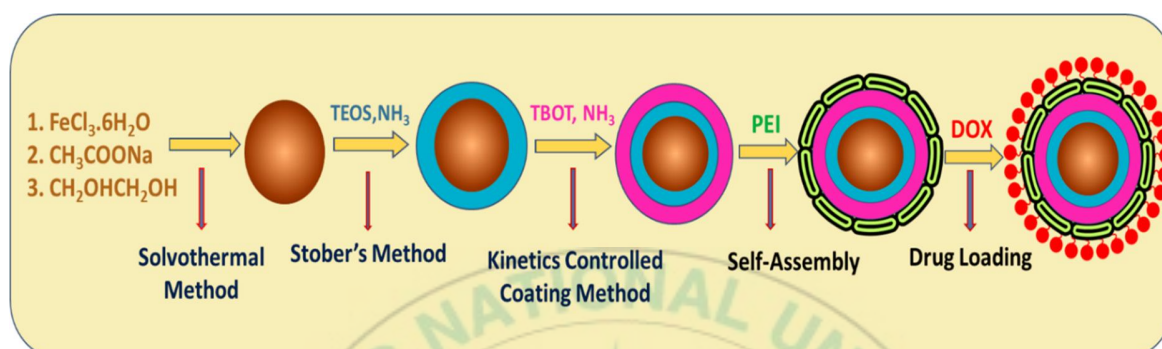
Owing to the unique properties of pristine Fe_3O_4 nanoparticles, large surface area, excellent biocompatibility, high magnetic saturation, thermal stability, controllable dimensions, and strong adsorption ability they exhibit good application prospect in biomedical fields. On the contrary, the pristine Fe_3O_4 nanoparticles are highly reactive and to provide platform for further functionalization surface silanol groups of SiO_2 are used [45]. Titanium dioxide (TiO_2) has

prominent features such as biocompatibility, high chemical stability, nontoxicity, strong optical absorption and photocatalytic properties which enable wide applications in paints, food colorings, cosmetic and pharmaceutical industry. TiO_2 , when tailored with the nanosystem are suitable for different biomedical applications such as drug delivery, photokilling of tumor cells in photodynamic therapy, cell imaging, biosensors for biological assay and genetic engineering [46]. TiO_2 also has extraordinary antibacterial activity and are widely used in wound dressings, device coatings etc. [47]. TiO_2 act as photosensitizers by inducing reactive oxygen species formation (ROS) in photodynamic therapy, a non-invasive alternative treatment for cancer. TiO_2 coating directly on the Fe_3O_4 core may worsen the magnetic properties of the magnetic core so forming an intermediate silica layer between the magnetic core and TiO_2 shell is considered as a promising approach [48].

The surface modification by PEI polymer increase the hydrophilicity, biocompatibility and internalization efficiency. The PEI can self-assemble on the magnetic nanoparticles to protect from aggregation and favor targeted drug delivery. PEI is a pH sensitive polymer due to active amino groups which promote changing their properties in different physiological environments. In acidic pH tumor environment, the PEI polymers undergo a pH-dependent phase transition resulting in the release of the loaded drugs through polymer layer destabilizing properties. PEI functionalization maintain the therapeutic efficacy of the drugs. Moreover the strong positive charge in PEI is beneficial for cellular internalization of and cleaved only after entering the cell. PEI can bind to the negative proteoglycan on cell membranes and mediate the uptake process through electrostatic interactions. Doxorubicin (DOX), an antitumor antibiotic, was non-covalently conjugated to PEI polymer nanoparticles to induce controlled payload delivery into the target sites in the presence of pH stimuli. By physiological pH the DOX is probably conjugated to the PEI shell but in acidic pH 5 and below, protonation of the drug occurs resulting in release of the physisorbed drug. [49, 50].

Herein, we present a straightforward and versatile method to synthesize PEI-DOX $\text{Fe}_3\text{O}_4@SiO_2@TiO_2$ core-shell nanoparticles for potential chemotherapy applications. The synthesized core-shell system combines the magnetic Fe_3O_4 core, SiO_2 interlayer, TiO_2 shell and the PEI shell with DOX payload. It is important to emphasize that the branched-PEI provides high potential to be applied as a nanovehicle to carry chemotherapeutic agents. The drug loading and

in vitro drug release behavior of the PEI-DOX@Fe₃O₄@SiO₂@TiO₂ core-shell nanoparticles were evaluated at different pH conditions. Additionally, the cellular uptake and the in vitro anticancer efficacy of the PEI-DOX@Fe₃O₄@SiO₂@TiO₂ core-shell nanoparticles were investigated using the MDA-MB-231 breast cancer cell line. The schematic illustration describes the logical step wise synthesis of PEI-DOX@Fe₃O₄@SiO₂@TiO₂ core-shell nanoparticles following various methods and its use in chemotherapy applications.



Scheme 3 Schematic illustration of the design of PEI@Fe₃O₄@SiO₂@TiO₂/DOX core-shell nanoparticles for drug release under pH stimuli in cancer therapy.

EXPERIMENTAL SECTION

2.1. Chemicals and reagents

Iron (III) chloride (FeCl₃.6H₂O), ethylene glycol, anhydrous sodium acetate, trisodium citrate, tetraethyl orthosilicate (TEOS), titanium (IV) butoxide, ammonium hydroxide (NH₄ OH, 28 wt%), sodium hydroxide, branched polyethyleinimine and doxorubicin hydrochloride were purchased from Sigma Aldrich (USA). Absolute ethanol was purchased from Daejung Chemicals. Phosphate-buffered saline (PBS), fetal bovine serum, Dulbecco's modified Eagle's medium (DMEM), streptomycin, 1× trypsin, and penicillin, were purchased from HyClone (South Logan, UT, USA). 3-(4,5-dimethylthiazol-2-yl)-2,5-diphenyltetrazolium bromide (MTT), acridine orange (AO), propidium iodide (PI) were also obtained from Sigma-Aldrich (St. Louis, MO, USA). All the reagents were used of analytical grade and used without further purification.

2.2 Synthesis of the nanocarrier

2.2.1 Synthesis of magnetic Fe₃O₄ nanoparticles.

The magnetic Fe₃O₄ nanoparticles were synthesized through a previously reported solvothermal approach with some modification [51]. Typically, 1 mmol of ferric chloride was dissolved in 15 mL of ethylene glycol and stirred until the solution becomes clear yellow. Subsequently, 0.9 g of sodium acetate was added and stirred for 2 h. After, 0.12 g trisodium citrate was added and the suspension was stirred at room temperature for 4 h. The obtained homogenous brown dispersion was transferred into a Teflon-lined stainless steel autoclave (100 mL capacity) and heated at 200 °C for 8 h. The obtained black magnetic nanoparticles were washed with water and ethanol and then finally dried at 70 °C. The synthesized Fe₃O₄ nanoparticles were highly hydrophilic and could be readily dispersed in water and ethanol.

2.2.2 Synthesis of Fe₃O₄@SiO₂ core-shell nanoparticles.

The immediate shell (interlayer) of silica was formed through a modified Stober method. In this typical process, firstly, 0.25 g of the as-prepared Fe₃O₄ nanoparticles were dispersed in 80 mL of absolute ethanol, 20 mL deionized water and 6 mL ammonia mixture and ultrasonicated for 15 mins to acquire well dispersed nanoparticles. Secondly, 0.6 g of TEOS was added drop wise and vigorously stirred for 4 h. The obtained product was collected by external magnet and washed with water and ethanol and then dried at 70 °C for further use.

2.2.3 Synthesis of titania outer-shell over the Fe₃O₄@SiO₂ core-shell nanoparticles by kinetics controlled coating method.

About 0.1g Fe₃O₄@SiO₂ particles were dispersed in absolute ethanol, (100 mL) and concentrated ammonia solution 0.3 mL (28 wt%) was added under ultrasonic agitation for about 15 min. About 0.75 mL titanium (IV) butoxide solution was added dropwise within 5 min and constantly stirred at 45°C for 24h. Finally, the dried at 100°C overnight. The synthesized, Fe₃O₄@SiO₂@ TiO₂ core-shell nanoparticles are hydrophobic [52].

2.2.4 PEI grafting onto the Fe₃O₄@SiO₂@TiO₂ core-shell nanoparticles

The formed Fe₃O₄@SiO₂@TiO₂ core-shell nanoparticles are hydrophobic and further modification is possible after grafting PEI hydrophilic polymer for drug loading and to improve the biocompatibility of the nanocarrier system. About 0.25 g of PEI was dissolved in 50 mL of distilled water under ultrasonication for 15 min. About 0.2 g Fe₃O₄@SiO₂@TiO₂ nanoparticles was dispersed in PEI solution under sonication for 2 hr. The suspension was rinsed with deionized water to remove excess or unreacted PEI [53].

2.3. Characterizations

The synthesized Fe₃O₄@SiO₂@TiO₂ and PEI Fe₃O₄@SiO₂@TiO₂ core-shell nanoparticles were characterized using various techniques. The wide-angle X-ray diffraction (XRD) patterns of the samples was measured using X' Pert MPD system, Philips, Almelo, Netherlands) X-ray diffractometer with Cu K_α radiation. The transmission electron microscope (TEM) (JEOL JEM-2100) equipped with an accelerated voltage of 200 kV, with an energy dispersive X-ray spectroscope (EDX) with an accelerator voltage of 200 kV. The scanning electron microscopy (SEM) images were measured on JEOL JEM 2010) microscope with accelerating voltage of 150 kV. UV-visible absorption spectra were recorded using a Shimadzu UV- 2450 spectrophotometer in a quartz cuvette with an optical path of 1 cm length. Fourier transform infrared (FTIR) spectroscopy was performed with a PerkinElmer Spectrum 100 using KBr pelleting method. Particle size distribution of the sample was measured by dynamic light scattering using Beckman Coulter, LS 13320 particle size analyzer. Thermogravimetric (TG) analysis was done on a TGA, Perkin-Elmer Pyris Diamond in the temperature range 50 °C to 700 °C with a heating rate 10 °C/min under air atmosphere. The evolution of the zeta potential of the nanoparticles were analyzed using a Zetasizer Nano ZS equipped with a He-Ne laser at 633 nm from Malvern.

2.4 DOX loading onto the PEI@Fe₃O₄@SiO₂@TiO₂ core-shell nanoparticles

DOX, an anthracycline topoisomerase inhibitor, binds to nucleic acids and prevents DNA replication. To circumvent the DOX efflux, the drug DOX was loaded on to the PEI Fe₃O₄@SiO₂@TiO₂ surface by a labile non-covalent bond, cleavable at strong acidic pH and by

electrostatic interaction between the amine molecules of the drug and the amine and hydroxyl part of the PEI@Fe₃O₄@SiO₂@TiO₂. About 2 mL aqueous solution of DOX (10 mg/mL) was added to 50 mg/mL of PEI@Fe₃O₄@SiO₂@TiO₂ nanoparticles suspended in distilled water. The reaction mixture was kept in magnetic stirring in the dark conditions for 24 hr. After DOX loading, the samples were magnetically separated, washed and dried at 60 °C. The PEI@Fe₃O₄@SiO₂@TiO₂/DOX can be well dispersed in water to act as drug delivery platform to deliver anticancer drug, DOX. The amount of drug grafted to the core-shell nanoparticles is measured by UV spectrometer by the characteristic absorption peak of DOX at 490 nm. UV – visible absorbance of Fe₃O₄@SiO₂@TiO₂ showed a red shift after DOX loading, which is evident that the Fe₃O₄@SiO₂@TiO₂ core shell surface was modified by DOX ligand by non-covalent complexation and physisorption on the surface of the core-shell nanoparticles. The drug encapsulation efficiency was calculated as follows: [Encapsulation efficiency (%) = Mass of drug in nanoparticles / Mass of drug injected × 100]. The loaded DOX was estimated to be approximately 55%. The maximum 55% drug loading efficiency was achieved due to the presence of large content of drug interacting amine and hydroxyl groups in the core-shell.

2.5. *In vitro* pH- stimuli responsive DOX release experiments

For the *in vitro* drug release experiments, about 50 mg Fe₃O₄@SiO₂@TiO₂/DOX core-shell nanoparticles was added to 25 ml of PBS buffer and the mixture was shaken at 37 °C in a water bath. The pH of the buffer medium was adjusted to pH 7.2, pH 5.4 or pH 4.0 respectively. At different time intervals, 1 ml of aliquots were taken and replaced with 1 ml of fresh PBS solution. The aliquot was analyzed using UV-visible spectrophotometer at 490 nm for DOX to evaluate the drug release efficiency at different pH conditions. Also, the drug release experiments were performed in triplicate for each samples.

2.6. *In vitro* cytotoxicity assay

The *in vitro* MTT assay analysis of the Fe₃O₄@SiO₂@TiO₂ core-shell nanoparticles without DOX loading and the DOX-loaded PEI@Fe₃O₄@SiO₂@TiO₂/DOX core-shell nanoparticles were determined using MDA-MB-231 cell line. For this study, the cells were cultured in 96-well plate with a density of 1×10^4 cells per well and incubated with the samples at different concentrations (20–100 µg/mL, respectively) and incubated for 24 h at 37 °C. Next, about 20 µL of MTT reagent

solution was added to each well and further incubated for 4 h. Then, the existing medium in each well was replaced by adding dimethyl sulfoxide (DMSO, 200 μ L) and gently shaken for 15 min. The absorbance value was measured at 570 nm. The cell viable percentage was calculated by using the equation below.

$$\text{Cell viability (\%)} = \frac{(\text{OD}_{\text{treated}})}{(\text{OD}_{\text{control}})} \times 100$$

$\text{OD}_{\text{treated}}$ indicates the cells treated with without DOX loading $\text{Fe}_3\text{O}_4@\text{SiO}_2@\text{TiO}_2$ and the DOX-loaded $\text{Fe}_3\text{O}_4@\text{SiO}_2@\text{TiO}_2/\text{DOX}$. $\text{OD}_{\text{control}}$ indicates the control cells treated without nanoparticles.

2.7. *In vitro* cellular uptake study

The *in vitro* cell uptake behavior of the $\text{PEI}@\text{Fe}_3\text{O}_4@\text{SiO}_2@\text{TiO}_2/\text{DOX}$ core-shell nanoparticles was determined using fluorescence microscopic analysis. To perform this experiment, MDA-MB-231 cells were seeded in 6-well plate and grown in DMEM for 24 h. Then, the cells were treated with the varying concentrations of $\text{Fe}_3\text{O}_4@\text{SiO}_2@\text{TiO}_2$ and PEI-DOX $\text{Fe}_3\text{O}_4@\text{SiO}_2@\text{TiO}_2$ nanoparticles and further incubated for 4 h. After treatment, the sample treated cells were fixed with 4% paraformaldehyde for 15 min, the medium was removed, and the dishes were washed thrice with fresh PBS to remove the unattached nanoparticles. The fluorescence cell images were obtained by using fluorescence microscopy.

3. RESULTS AND DISCUSSION

XRD was used to investigate the crystal structure and phase purity of the $\text{Fe}_3\text{O}_4@\text{SiO}_2@\text{TiO}_2$ core-shell nanoparticles. Figure 9 (a-d) shows the XRD patterns for the synthesized pristine Fe_3O_4 nanoparticles, $\text{Fe}_3\text{O}_4@\text{SiO}_2$ nanoparticles, $\text{Fe}_3\text{O}_4@\text{SiO}_2@\text{TiO}_2$ and $\text{PEI}@\text{Fe}_3\text{O}_4@\text{SiO}_2@\text{TiO}_2$ core-shell nanoparticles. In Figure 9 (a), the pristine Fe_3O_4 nanoparticles shows sharp crystalline peaks (at 2θ : 30.7, 35.9, 43.4, 53.9, 58.4 and 63.2 corresponding to the XRD reflection planes of (220), (311), (400), (422), (511) and (440),

respectively. The intensity of the diffraction peak of (311) plane is stronger than the other peaks and the results indicate that the synthesized Fe_3O_4 nanoparticles diffraction peaks are consistent with the inverse spinel structure of magnetite (JCPDS 85-1436). As in Figure 9 (b), the coating of amorphous silica layer on Fe_3O_4 surface did not change the structure of Fe_3O_4 but only reduced the peak intensity of Fe_3O_4 . The $\text{Fe}_3\text{O}_4@\text{SiO}_2@\text{TiO}_2$ core-shell nanoparticles as in Figure 9 (c) shows no additional peaks and weakened intensity of the peaks indicate the shielding effect of amorphous TiO_2 coated onto the $\text{Fe}_3\text{O}_4@\text{SiO}_2$ surface. The lack of clear titania diffraction peaks can be due to the very thin titania layer also mentioned in other studies. As observed in the XRD pattern of d, the results confirm that the amorphous SiO_2 , amorphous TiO_2 and PEI coating over the magnetite nanoparticles do not stimulate any phase transition and ensure the high purity of the synthesized $\text{PEI}@\text{Fe}_3\text{O}_4@\text{SiO}_2@\text{TiO}_2$ core-shell nanoparticles. The peak broadening of the XRD pattern in Figure 9 (b, c and d) is a clear evidence for the formation of ultrasmall nanocrystals. Therefore, the XRD patterns of the $\text{Fe}_3\text{O}_4@\text{SiO}_2$, $\text{Fe}_3\text{O}_4@\text{SiO}_2@\text{TiO}_2$, $\text{PEI}@\text{Fe}_3\text{O}_4@\text{SiO}_2@\text{TiO}_2$ nanoparticles have diffraction peaks similar to those of the parent Fe_3O_4 core without any phase change.

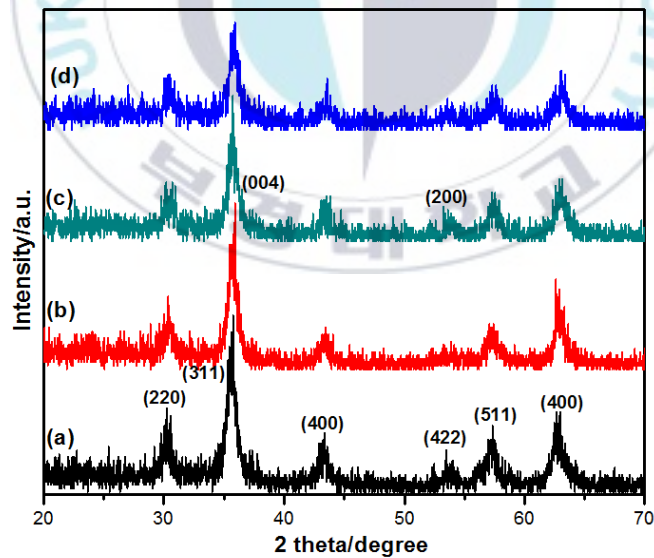


Figure 9 Wide-angle XRD patterns of (a) pristine Fe_3O_4 nanoparticles, (b) $\text{Fe}_3\text{O}_4@\text{SiO}_2$ (c) $\text{Fe}_3\text{O}_4@\text{SiO}_2@\text{TiO}_2$ (d) $\text{PEI}@\text{Fe}_3\text{O}_4@\text{SiO}_2@\text{TiO}_2$ core-shell nanoparticles.

FT-IR analysis was performed for the pristine Fe_3O_4 , $\text{Fe}_3\text{O}_4@\text{SiO}_2$, $\text{Fe}_3\text{O}_4@\text{SiO}_2@\text{TiO}_2$ and PEI-DOX $\text{Fe}_3\text{O}_4@\text{SiO}_2@\text{TiO}_2$ nanoparticles in the range of 500-4000 cm^{-1} and are shown in Figure 10 (a-d). The FTIR spectra of pristine Fe_3O_4 in Figure 10 (a) shows a broad and strong absorption peak at approximately 572 cm^{-1} that confirms the presence of Fe-O vibration band and the weak vibration monitored at 1077 cm^{-1} is characteristic of surface Fe-OH groups stretching within Fe_3O_4 nanoparticles. A broad peak at 3343 cm^{-1} represents the O-H stretching vibration with the presence of water molecules. The characteristic peaks at 2950 cm^{-1} can be assigned to the C-H group vibrations of propyl carbon chains due to the use of ethylene glycol and no other extra peaks were observed and this confirms the high purity of uncoated Fe_3O_4 nanoparticles. After silica coating onto the Fe_3O_4 nanoparticles, the $\text{Fe}_3\text{O}_4@\text{SiO}_2$ nanoparticles show the vibration peaks at 1230 cm^{-1} and 997 cm^{-1} indicating the rocking vibrations of Si-O-Si network and presence of surface silanol (Si-OH) groups as observed in Figure 10 (b). The IR spectrum of $\text{Fe}_3\text{O}_4@\text{SiO}_2@\text{TiO}_2$ in Figure 10 (c) consists of four absorption bands, a broad band centered at 3313 cm^{-1} due to a stretching vibration of O-H groups linked to a TiO_2 surface, a narrower band at 1631 cm^{-1} was the scissoring vibration of the adsorbed water molecules, the typical Si-O-Ti bridging bonds at about 955 cm^{-1} and Ti-O-Ti bonds at 786 cm^{-1} . The asymmetric Si-O-Ti vibrating bonds ascribe to the incorporation of tetrahedrally coordinated Ti 4+ ions into the $\text{Fe}_3\text{O}_4@\text{SiO}_2$ matrix. In addition, the Figure 10 (d) shows the overlapped peak at is due to N-H stretching of PEI coating. Finally, the slight shifts, decreased intensity of the Fe-O bond, the N-H peak decreased intensity in curves b, c, and d in comparison with curve (a) notably suggests that the iron oxide core was totally covered by SiO_2 , TiO_2 and PEI polymer shells [54].

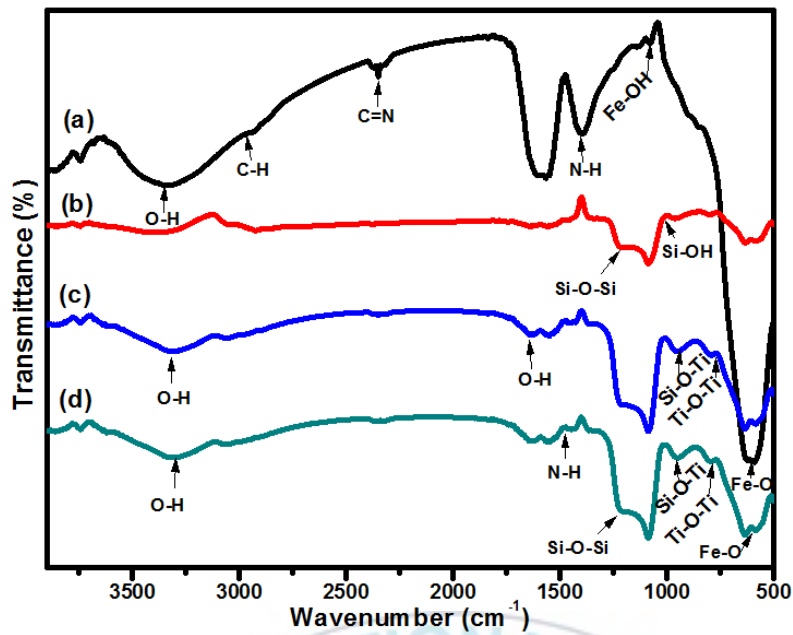


Figure 10 FTIR analysis of (a) Fe₃O₄ nanoparticles (b) Fe₃O₄@SiO₂ (c) Fe₃O₄@SiO₂@TiO₂ and (d) PEI-DOX Fe₃O₄@SiO₂@TiO₂ core-shell nanoparticles.

To quantify the coating percentage of silica, titania and PEI on the surface of Fe₃O₄ nanoparticles thermogravimetric (TG) analysis in inert (Nitrogen) atmosphere was performed. Figure 11 (a-c) display the TGA curves of Fe₃O₄@SiO₂, Fe₃O₄@SiO₂@TiO₂ and PEI coated Fe₃O₄@SiO₂@TiO₂ core-shell nanoparticles without DOX loading respectively. All the samples show four stage weight loss with temperature range from 100 °C to 700 °C. The initial weight losses of about 0.4 to 0.6 wt% at the temperature range, 100 °C is due to the evaporation of physisorbed water and solvents. At, 300 °C the Fe₃O₄@SiO₂, Fe₃O₄@SiO₂@TiO₂ and PEI@Fe₃O₄@SiO₂@TiO₂ core-shell nanoparticles show a second abrupt weight loss of about 1.2%, 6% and 7% due to the removal of labile oxygen -containing functional groups such as CO, CO₂ and H₂O. The third weight loss of about 9% and 16% at 500 °C was observed for Fe₃O₄@SiO₂@TiO₂ and PEI@Fe₃O₄@SiO₂@TiO₂ core-shell nanoparticles due to the decomposition of propyl carbon and amine units. The fourth stage weight loss occurs at 500 °C to 700 °C for the condensation of silica and titania network and decomposition of the carbon residues as indicated in curve a, b & c. Finally, the overall weight losses for the PEI@Fe₃O₄@SiO₂@TiO₂ core-shell nanoparticles was 19 wt%

which denotes the considerable amount of organic functional groups and PEI successfully incorporated to the magnetic core nanoparticles.

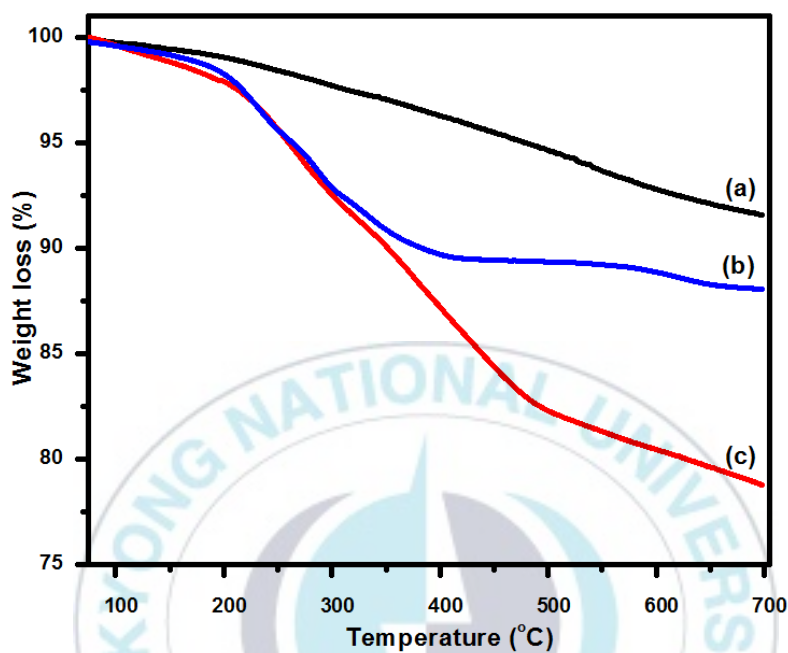


Figure 11 TGA profile curves of (a) $\text{Fe}_3\text{O}_4@\text{SiO}_2$ (b) $\text{Fe}_3\text{O}_4@\text{SiO}_2@\text{TiO}_2$ core-shell (c) PEI $\text{Fe}_3\text{O}_4@\text{SiO}_2@\text{TiO}_2$ core-shell nanoparticles without DOX loading.

The surface morphology of the $\text{Fe}_3\text{O}_4@\text{SiO}_2@\text{TiO}_2$ core-shell nanoparticles were also observed by FESEM analysis. As revealed in Figure 12 (a) the Fe_3O_4 nanoparticles possess a spherical structure with little rough surface and are well dispersed. After silica coating the surface becomes smooth, non-porous and the nanoparticles are aggregated to some extent forming necking of the silica layers as seen in Figure 12 (b). The newly formed silica layers are uniformly coated onto the magnetic core without homogenous nucleation and with abundant Si-OH groups on the surface, which provide reactive sites for further titania deposition. As in figure 12 (c), the $\text{Fe}_3\text{O}_4@\text{SiO}_2@\text{TiO}_2$ core-shell nanoparticles surface is rougher, more porous and the size of the spheres have been increased due to the deposition of small crystalline TiO_2 nanoparticles.

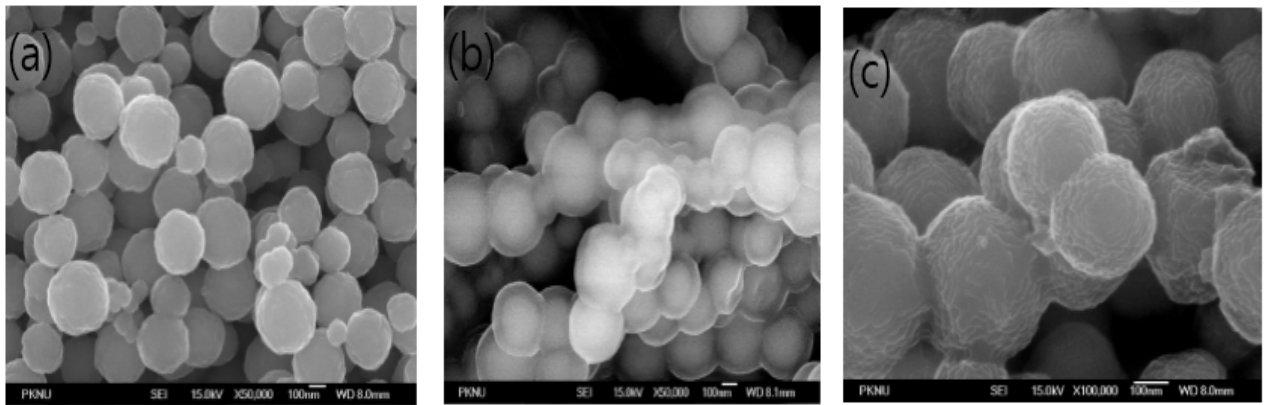


Figure 12 SEM images of (a) Fe_3O_4 nanoparticles (b) $\text{Fe}_3\text{O}_4@\text{SiO}_2$ nanoparticles and (c) $\text{Fe}_3\text{O}_4@\text{SiO}_2@\text{TiO}_2$ core-shell nanoparticles.

To get information about aforementioned core-shell structure, morphology of the PEI $\text{Fe}_3\text{O}_4@\text{SiO}_2@\text{TiO}_2$ nanoparticles were observed by FETEM analysis as shown in Figure 13 (a-d). The TEM image of pristine Fe_3O_4 nanoparticles in figure 13 (a) consists of uniform spherical shape nanocrystals with a few tiny nanoparticles and the inset is the magnified image of a single pristine Fe_3O_4 nanoparticle. Figure 13 (b) shows the morphology of $\text{Fe}_3\text{O}_4@\text{SiO}_2$ nanoparticles, with the magnetic core inside and a uniform non-porous silica layer outside. The regular spherical shape with the smooth surface and necking of the silica layers are due to the molecular scale level deposition of silica in the stober's sol gel process. Figure 13 (c) shows the morphology of $\text{Fe}_3\text{O}_4@\text{SiO}_2@\text{TiO}_2$ nanoparticles with the core-shell structure, the TiO_2 nanoparticles firmly anchored onto the surface of $\text{Fe}_3\text{O}_4@\text{SiO}_2$ nanoparticles by the kinetics controlled coating method. The $\text{Fe}_3\text{O}_4@\text{SiO}_2 @\text{TiO}_2$ nanoparticles shows rougher, crystalline nanoparticles less aggregated with more porous structure which imply that the silica middle layer influences the deposition of TiO_2 nanoparticles. However, the SiO_2 interlayer cannot be clearly differentiated from TiO_2 overlayer due to the densely deposited TiO_2 shell and their similar contrast.

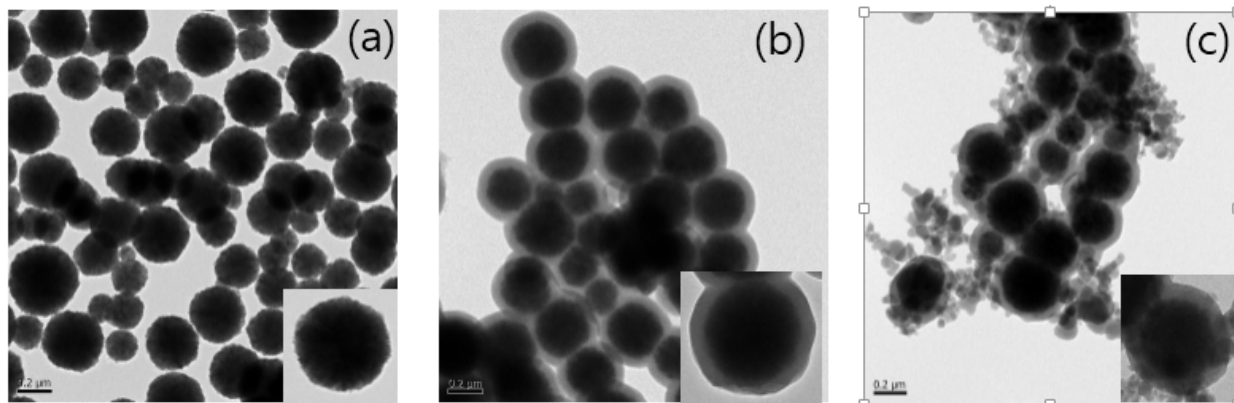


Figure 13 TEM images of the (a) Fe_3O_4 nanoparticles (b) $\text{Fe}_3\text{O}_4@\text{SiO}_2$ (c) $\text{Fe}_3\text{O}_4@\text{SiO}_2@\text{TiO}_2$ nanoparticles and the inset is the TEM of a single particle.

Figure 14 gives TEM EDS spectrum and mapping images of the $\text{Fe}_3\text{O}_4@\text{SiO}_2@\text{TiO}_2$ core-shell nanoparticles. As in Figure 14 (a), the peaks of Fe, O and Si come from $\text{Fe}_3\text{O}_4@\text{SiO}_2$ nanoparticles and the inset is their elemental composition. The $\text{Fe}_3\text{O}_4@\text{SiO}_2$ nanoparticles have 38.71 atomic ratio of iron, 25.73 atomic ratio of Silica and 35.56 atomic ratio of oxygen. As in Figure 14 (b) the peaks of Fe, O, Si in and Ti is from $\text{Fe}_3\text{O}_4@\text{SiO}_2@\text{TiO}_2$ core-shell nanoparticles. The $\text{Fe}_3\text{O}_4@\text{SiO}_2@\text{TiO}_2$ have 16.47 atomic ratio of iron, 14.80 atomic ratio of Silica, 15.59 atomic ratio of titania and 59.88 atomic ratio of oxygen. The EDS analysis confirms the elemental composition of $\text{Fe}_3\text{O}_4@\text{SiO}_2$ nanoparticles and $\text{Fe}_3\text{O}_4@\text{SiO}_2@\text{TiO}_2$ core-shell nanoparticles. It also suggests that no chemically stable contaminants are detected and the fabricated core-shell nanoparticles are pure.

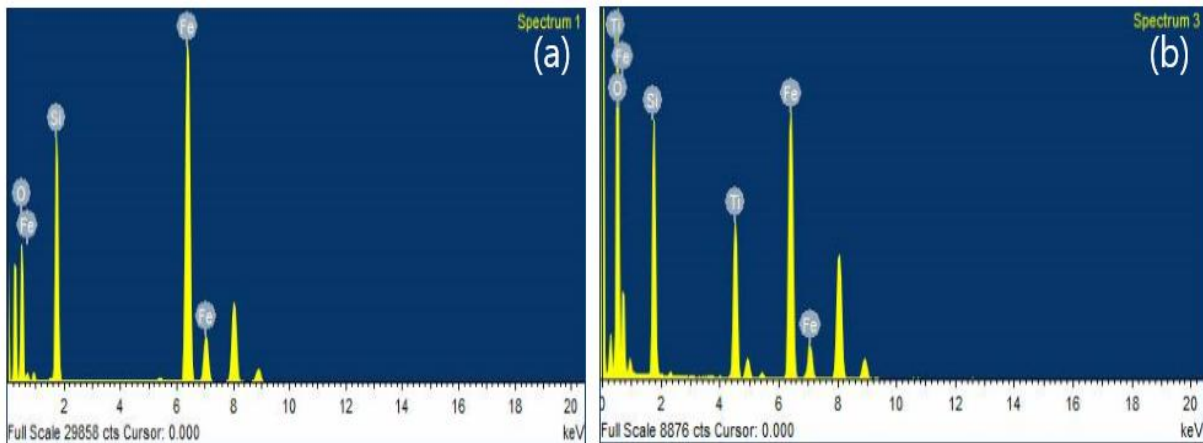
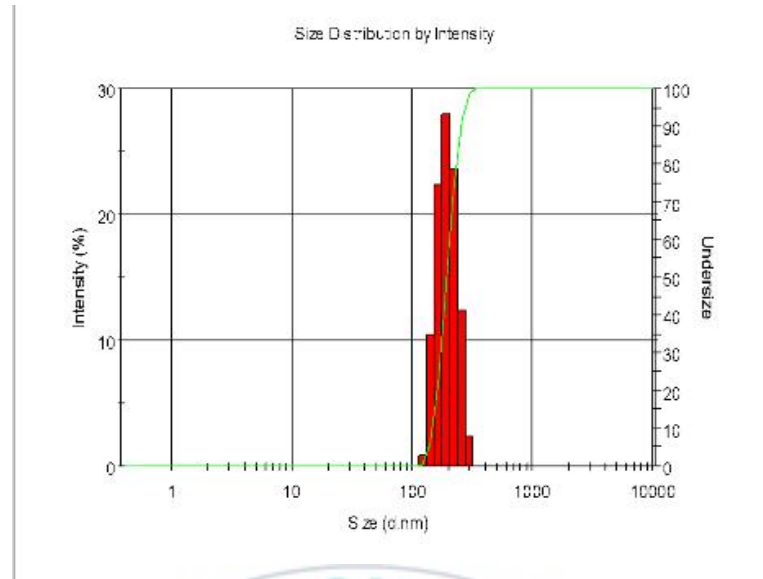


Figure 14 EDX analysis of (a) $\text{Fe}_3\text{O}_4@\text{SiO}_2$ nanoparticles and (b) $\text{Fe}_3\text{O}_4@\text{SiO}_2@\text{TiO}_2$ core-shell nanoparticles

The average particle size distribution and zeta potential measurement of the $\text{Fe}_3\text{O}_4@\text{SiO}_2@\text{TiO}_2$ nanoparticles were also estimated as shown in Figure 15. The average particle size of $\text{Fe}_3\text{O}_4@\text{SiO}_2@\text{TiO}_2$ core-shell nanoparticles were around 200 nm as shown in Figure 15 (A). The successful loading of DOX to the surface of $\text{Fe}_3\text{O}_4@\text{SiO}_2@\text{TiO}_2$ core-shell nanoparticles was evident by the difference in zeta potential (Fig 15 b) At pH 7.4, zeta potential of Fe_3O_4 , $\text{Fe}_3\text{O}_4/\text{SiO}_2$ and $\text{Fe}_3\text{O}_4/\text{SiO}_2/\text{TiO}_2$ were -7.29 mV, -11.44 mV, -23.43 mV respectively due to the abundant surface hydroxyl groups. At the same pH value, after DOX was loaded onto the core shell nanoparticles, the zeta potential was +3.09 mV due to the amine groups of DOX molecule indicating the adsorption of DOX onto the $\text{Fe}_3\text{O}_4@\text{SiO}_2@\text{TiO}_2$ core-shell nanoparticles by non-covalent bond and electrostatic interactions.

(A)



(B)

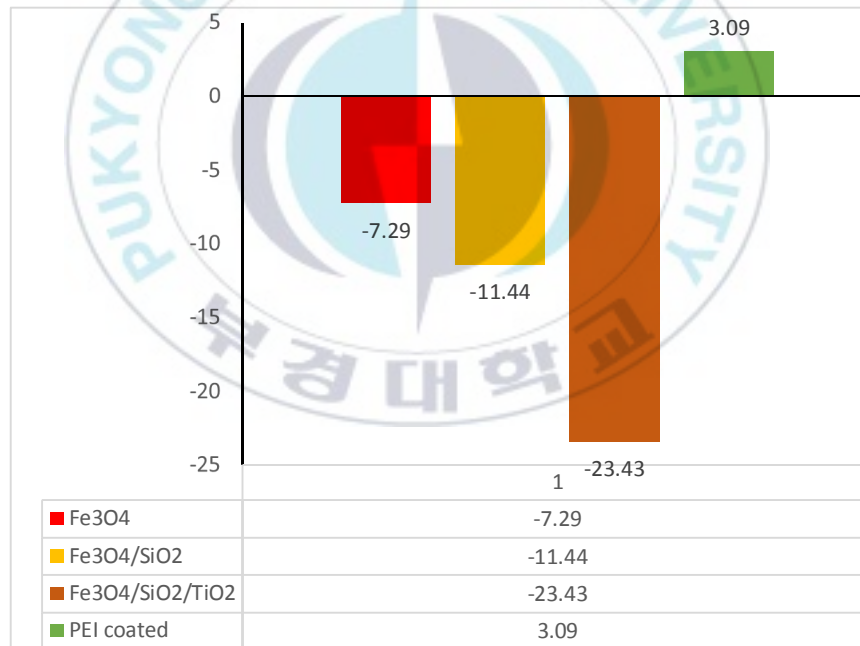


Figure 15 (A) Particle size distributions (DLS) of PEI@Fe₃O₄@SiO₂@TiO₂ core-shell nanoparticles and (B) Zeta potential of the PEI@Fe₃O₄@SiO₂@TiO₂ core-shell nanoparticles.

***In vitro* drug loading and release behavior of DOX**

The DOX molecule is electropositive due to the presence of daunosamine moiety and could be readily deposited on the amine rich surface of the PEI@Fe₃O₄/SiO₂/TiO₂ core-shell nanoparticles *via* electrostatic interactions. PEI with abundant terminal amino groups holds the drug and releases from the pores in a very controlled manner. To investigate the pH-responsive drug release behavior of PEI-DOX@Fe₃O₄@SiO₂@TiO₂ core-shell nanoparticles, three different pH conditions were employed specifically pH 7.2, pH 5.4 and pH 4.0. As shown in Figure 16, the cumulative DOX release rate was considerably low about 30 %, at 24 h under physiological pH 7.2. In contrary, PEI has the unique proton sponge effect, which buffers under acidic conditions and the DOX release rates were enhanced effectively. About, 60 % DOX were released at acidic pH conditions (pH 5.4) and 70 % DOX were released at pH 4.0 after 24 h. About 30% DOX release occurred at pH 7.4 due to the weakly adsorbed and surface adhered drug molecules. The enhanced release of about 60% and 70% occurred because of the dissolution and dissociation of PEI shell under acidic pH (pH 5.4 and pH 4.0) conditions and the protonation of the amine and hydroxyl groups of the DOX under acidic pH conditions. Therefore, the impregnated drug molecules with the Fe₃O₄@SiO₂@TiO₂ core-shell nanoparticles start to dissolve and diffuse out from the PEI@Fe₃O₄@SiO₂@TiO₂ core-shell nanocarrier pores. The overall drug release study results evidenced that the synthesized PEI@Fe₃O₄@SiO₂@TiO₂@DOX core shell nanoparticles has a great potential to be utilized as nanocarriers in loading and releasing DOX based on pH-responsive drug release mechanisms. Moreover, the intracellular tumor environment is more acidic than normal tissues, the PEI coating thereby favors targeted and controlled release of DOX.

Stimuli-responsive target and site-specific drug release are important factors for drug delivery nanosystems applied in the biomedical field. The DOX loading on porous nanosystem through electrostatic and hydrogen bonding interactions is a major advantage for pH controlled drug release mechanisms. The DOX release rate was highly increased with decreasing the pH range. As the intracellular tumor environment tends to become more acidic (< pH 5.5), as compared with the normal physiological environment (~pH 7.4) the PEI-DOX@Fe₃O₄@SiO₂@TiO₂ core-shell nanoparticles have great potential for pH dependent DOX release. Therefore the PEI-DOX@Fe₃O₄@SiO₂@TiO₂ core-shell nanoparticles system can readily transfer the loaded DOX into

cancer cells, increasing the cytotoxicity levels. Additionally, the acid sensitive PEI shell can be cleaved only after cellular internalization ensuring safe delivery of DOX to the cell nucleus.

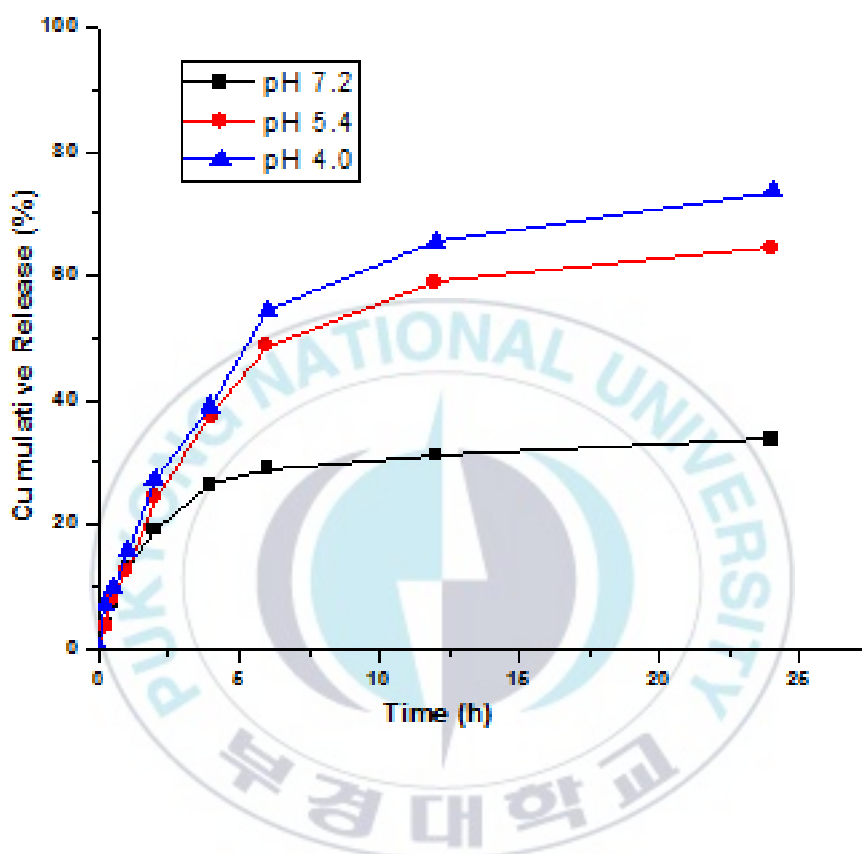


Figure 16 *In vitro* drug release profiles of (a) DOX drug at different pH conditions (pH 7.2, pH 5.4 and 4.0, respectively) in PBS buffer medium.

Cell culture conditions

MDA-MB-231 human breast cancer cells (Korea Cell Line Bank, Seoul, South Korea) were cultured and maintained in Dulbecco's Modified Eagle's Medium (DMEM) supplemented with 10% FBS, 100 U mL⁻¹ penicillin and 100 µg mL⁻¹ streptomycin. The cell cultures were maintained in a 5% CO₂ incubator at 37 °C in a humidified atmosphere.

***In vitro* cellular toxicity**

The cytotoxicity of the nanoparticles is crucial for the chemotherapy application. The cytotoxic effect of $\text{Fe}_3\text{O}_4@\text{SiO}_2@\text{TiO}_2$ and $\text{Fe}_3\text{O}_4@\text{SiO}_2@\text{TiO}_2/\text{DOX}$ core-shell nanoparticles was evaluated by MTT cell viability assay. Human breast cancer cells (MDA-MB-231) were seeded into a 96-well microplate at a density of 1×10^4 cells/well in DMEM medium and were incubated overnight for cell adhesion. The cell culture media was replaced with fresh medium containing varying concentrations of the $\text{Fe}_3\text{O}_4@\text{SiO}_2@ \text{TiO}_2$ (20, 40, 60, 80 and 100 $\mu\text{g}/\text{mL}$) for 24h at 37 °C under 5% CO_2 . 100 μL of MTT containing DMEM medium (0.5 mg/mL) was added to each well and cultured for 4 h at 37 °C. Finally, after removing the existing medium, 100 μL of DMSO was added to each well to dissolve the purple formazan. After 15 min, the absorbance of the solution was measured at 570 nm using a microplate reader (BioTek, PowerWave XS2, Winooski, VT, USA). The relative cell viability percentage was calculated by the following equation.

$$\text{Cell viability (\%)} = \text{Absorbance of treated cells} / \text{Absorbance of control cells} * 100$$

As seen in Figure 17 the MTT assay reveals that the $\text{PEI}@\text{Fe}_3\text{O}_4@\text{SiO}_2@\text{TiO}_2$ nanoparticles showed low cytotoxicity (> 80 % viability remained) at concentrations upto 80 $\mu\text{g}/\text{mL}$ and 100 $\mu\text{g}/\text{mL}$ showed more toxicity > 66% so 20-80 $\mu\text{g}/\text{mL}$ concentration of $\text{Fe}_3\text{O}_4@\text{SiO}_2@\text{TiO}_2$ nanoparticles are safe and could be used as a biocompatible nanocarrier to deliver anti-cancer drugs like DOX. In contrast, the cells treated with the $\text{PEI-DOX}@\text{Fe}_3\text{O}_4@\text{SiO}_2@\text{TiO}_2$ core-shell nanoparticles showed a significant concentration dependent toxicity even at the lowest concentration of 20 $\mu\text{g}/\text{mL}$. When the concentration of the $\text{PEI-DOX}@\text{Fe}_3\text{O}_4@\text{SiO}_2@\text{TiO}_2$ core-shell nanoparticles is increased from 20 $\mu\text{g}/\text{mL}$ to 100 $\mu\text{g}/\text{mL}$, the cytotoxicity level increased (26.47 % viability only remained) at concentrations upto 100 $\mu\text{g}/\text{mL}$ due to the excellent tumoricidal efficacy of DOX. This result implies that the $\text{Fe}_3\text{O}_4@\text{SiO}_2@\text{TiO}_2$ nanoparticles system could be utilized as an effective biocompatible nanocarrier for the targeted delivery of DOX to induce cell death in cancer therapeutics.

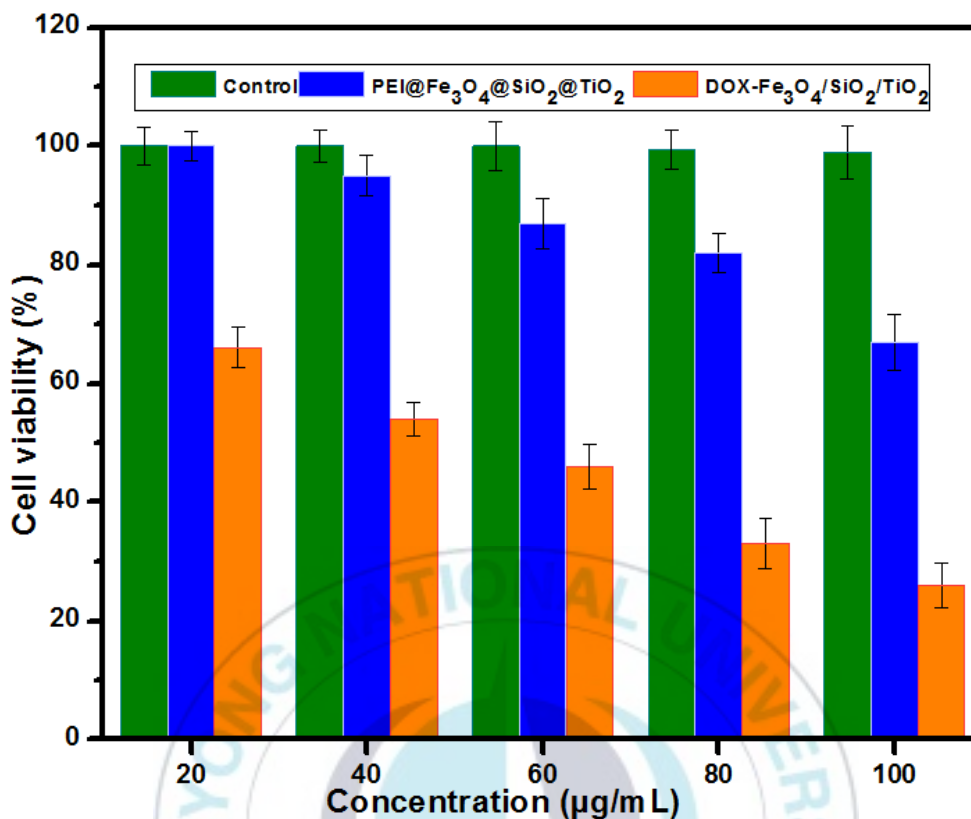


Figure 17 MTT assay of cells treated with Fe₃O₄@SiO₂@TiO₂ and PEI Fe₃O₄@SiO₂@TiO₂/DOX particles at various concentration.

The trypan blue stain is used to determine cell viability and to confirm the biocompatibility of the synthesized Fe₃O₄@SiO₂@TiO₂ core-shell nanoparticles. It is based on the principle that live cells possess intact cell membranes that exclude the trypan blue, whereas dead cells do not. So, a viable cell has a clear cytoplasm and a non-viable cell has a blue cytoplasm. Thus, the trypan blue stain helps to differentiate the morphology of live cells from dead cells. For this assay, MDA-MB-231 cells were cultured at a density of 1×10^5 cells/well in DMEM medium at 37°C. After the cells reached 80% confluence, the cells were treated with 80 µg/mL of the sample for 4 hrs. The cells were then allowed to stain with 0.4% trypan blue for 3-5 min. Finally, after two times washing with PBS, cells were observed under the bright field microscope. The live cells easily exclude the stain and appear as clear cells but the dead cells retain the stain and appear blue. As indicated in Figure 18 (a) shows the control cells, all viable with good morphology (b) the cells after incubation with 100 µg/mL of the Fe₃O₄@SiO₂@TiO₂ nanoparticles shows negligible toxicity demonstrating

biocompatibility of the synthesized core shell nanoparticles and (c) the cells after incubation with 20 $\mu\text{g/mL}$ of the PEI-DOX $\text{Fe}_3\text{O}_4@\text{SiO}_2@\text{TiO}_2$ nanoparticles shows nearly 40% of toxicity demonstrating the enhanced anti-cancer efficiency of the $\text{Fe}_3\text{O}_4@\text{SiO}_2@\text{TiO}_2/\text{DOX}$ core-shell nanoparticles even at minimum concentration against the MDA-MB-231 breast cancer cells.

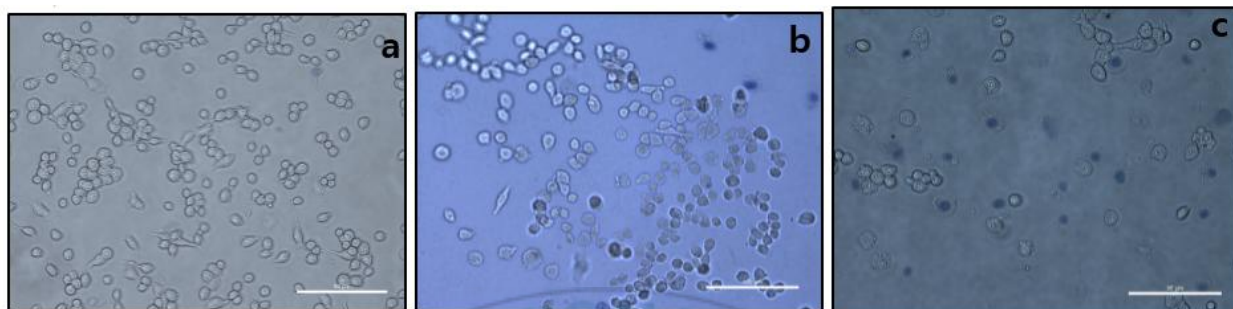


Figure 18 Trypan blue cell viability of MDA MB-231 cells incubated (a) without nanoparticles as Control (b) $\text{Fe}_3\text{O}_4@\text{SiO}_2@\text{TiO}_2$ treated cells with the fixed concentration 80 $\mu\text{g/mL}$ and (c) 20 $\mu\text{g/mL}$ PEI $\text{Fe}_3\text{O}_4@\text{SiO}_2@\text{TiO}_2/\text{DOX}$ treated cells respectively. Scale bar = 50 μm .

4. Conclusion

In summary, we have synthesized PEI@ $\text{Fe}_3\text{O}_4@\text{SiO}_2@\text{TiO}_2/\text{DOX}$ core-shell nanoparticles, which embedded a Fe_3O_4 core, SiO_2 interlayer and TiO_2 shell loaded with DOX for potential chemotherapy applications. The fabricated PEI-DOX $\text{Fe}_3\text{O}_4@\text{SiO}_2@\text{TiO}_2$ core-shell nanoparticles exhibit good thermal stability and high drug encapsulation efficiency due to the combined magnetic properties of Fe_3O_4 core, porosity, high drug loading properties of acid cleavable PEI shell. The enhanced 70 % DOX release at acidic pH 4.0 and 60% DOX release at acidic pH 5.4 conclude that the PEI@ $\text{Fe}_3\text{O}_4@\text{SiO}_2@\text{TiO}_2$ DOX core-shell nanoparticles have a great potential to be utilized as nanovehicles in loading and controlled release of anti-cancer drugs based on acidic pH-responsive drug release mechanisms. The MTT assay confirm that the synthesized $\text{Fe}_3\text{O}_4@\text{SiO}_2@\text{TiO}_2$ core-shell nanoparticles are biocompatible and non-toxic while the PEI DOX $\text{Fe}_3\text{O}_4@\text{SiO}_2@\text{TiO}_2$ core-shell nanoparticles demonstrate higher cell toxicity in killing human breast cancer cells.

Chapter 4.

Conclusion

The primary motivations of this research are the development of magnetic based nanomaterials for drug delivery applications. My research focused on the synthesis, functionalization and characterization of magnetic based nanomaterials and their applications in biomedical field. My research accomplishments are divided into two phases as mentioned in 2 chapters.

In chapter 2, I have described the preparation of magnetic hydroxyapatite which investigated in detail the formation of CaP shell suitable for the delivery of both hydrophilic and hydrophobic drugs. The chapter 3 depicts the preparation of magnetic core-shell structure nanoparticles loaded with a doxorubicin, a chemotherapeutic drug for targeted pH stimuli responsive drug delivery applications.

This research not only provides the basis for the development of new magnetic based nanomaterials but also for the expansion in practical applications. Further studies should preferably aim for flexible synthesis of magnetic based nanomaterials by tuning the structural properties.

References

- [1] M. Khatami, H.Q. Alijani, M.S. Nejad and R. S. Varma, *Appl. Sci.* 2018, **8**, 1-17.
- [2] H.M. Williams, *Biohorizons*. 2017, **10**, 1–10.
- [3] E.S. Lee, Z.G. Gao, Y.H Bae, *J. Control. Release*, 2008, **132**, 164–70.
- [4] Q. Yang, S.H Wang, P.W. Fan, L.F. Wang, Y. Di, K.F. Lin, *Chem Mater*. 2005, **17**, 5999 – 6003.
- [5] X.J. Kang, Z.Y. Cheng, D.M. Yang, P.A. Ma, M.M. Shang, C. Peng, *Adv. Funct. Mater.* 2012, **22**, 1470–81.
- [6] C. Po-Jung, H. Shang-Hsiu, H. Chi-Sheng, C. You-Yin, L. Dean-Mo, C. San-Yuan, *J. Mater. Chem*, 2011, **21**, 2535-2543.
- [7] H. Qianjun, G. Yu, Z. Lingxia, Z. Zhiwen, G. Fang, J. Xiufeng, *Biomaterials*, 2011, **32**, 7711 - 7720.
- [8] O.V. Salata, *J. Nanobiotechnol.*, 2004, **2**, 1-16.
- [9] S.C. Loo, T. Moore, B. Binak, F. Alexis, *Current Pharm Biotechnol.*, 2010, **11**, 333-342.
- [10] M. Motskin, D.M. Wright, K. Muller, N. Kyle, T.G. Gard, A.E. Porter, *Biomaterials*, 2009, **30**, 3307-17.
- [11] R. Stefani, G. Esposito, B. Zanotti, C. Iaccarino, M.M. Fontanella, F. Servadei, *Surg. Neurol. Int.* 2013, **4**, 12-20.
- [12] D.R. Jordan, S.M. Munro, S. Brownstein, S.M. Gilberg, S.Z. Grahovac, *Ophthal Plant Reconstr. Surg.* 1998, **14**, 244-249.
- [13] R. Karunamoorthi, G.S. Kumar, A.I. Prasad, R.K. Vatsa, A. Thamizhavel, E.K. Girija. *J Am Ceram Soc.* 2014, **97**, 1115–1122.
- [14] S.V. Dorozhkin, M. Epple, *Angew. Chem. Int. Ed.* 2002, **41**, 3130-3146.
- [15] V. Sokolova, T. Knuschke, J. Buer, A.M. Westendorf, M. Epple, *Acta Biomater*, 2011, **7**, 4029-36.
- [16] J. Li, Y.C. Chen, Y.C. Tseng, S. Mozumdar, L. Huang. *J. Control. Release*, 2010, **142**, 416-21.
- [17] S. Bose, S. Tarafder, *Acta Biomater*, 2012, **8**, 1401-21.
- [18] H.J. Lee, S.E. Kim, I.K. Kwon, C. Park, C. Kim, J. Yang, *Chem. Commun.*, 2010, **46**, 377-9.
- [19] C.H. Yeo, S.H.S. Zein, A.L. Ahmad, D.S. McPhail. *Ceram. Int.*, 2012, **38**, 561-70.
- [20] C. Yurong, P. Haihua, X. Xurong, H. Qinghong, L. Ling, T. Ruikang. *Chem. Mater.* 2007, **19**, 129-131.
- [21] J. Dobson, *Gene Ther.*, 2006, **13**, 283–287.
- [22] F. Sonvico, C. Dubernet, P. Colombo and P. Couvreur, *Curr. Pharm. Des.*, 2005, **11**, 2095–2105.
- [23] C. Xu and S. Sun, *Polym. Int.*, 2007, **56**, 821–826.
- [24] H. Gu, P. L. Ho, K. W. Tsang, L. Wang and B. Xu, *J. Am. Chem. Soc.*, 2003, **125**, 15702–

15703.

- [25] Z. Teng, J. Li, F. Yan, R. Zhao and W. Yang, *J. Mater. Chem.*, 2009, **19**, 1811–1815.
- [26] J. H. Ke, J. J. Lin, J. R. Carey, J. S. Chen, C. Y. Chen and L. F. Wang, *Biomaterials*, 2010, **31**, 1707–1715.
- [27] S. Liu, B. Jia, R. Qiao, Z. Yang, Z. Yu, Z. Liu, K. Liu, J. Shi, H. Ouyang, F. Wang and M. Gao, *Mol. Pharmacol.*, 2009, **6**, 1074–1082.
- [28] Y. Lu, Y. Yin, B.T. Mayers, Y. Xia, *Nano Letters*, 2002, **2**, 183–186.
- [29] W. Wu, Q. He and C. Jiang, *Nanoscale Res. Lett.* 2008, **3**, 397-415.
- [30] M.S. Moorthy, D.-J. Seo, H.-J. Sung, S.S. Park and C.-S. Ha, *J. Mater. Chem. A*, 2013, **1**, 12485-12496.
- [31] W.-M. Li, S.-Y. Chen, D.-M. Liu, *Acta Biomaterialia*, 2013, **9**, 5360–5368.
- [32] G. Bharath, A. Jagadeesh Kumar, K. Karthick, D. Mangalaraj, C. Viswanathan and N. Ponpandian, *RSC Adv.*, 2014, **4**, 37446-37457.
- [33] S.V. Dorozhkin, M. Epple, *Angew. Chem. Int. Ed.*, 2002, **41**, 3130–46.
- [34] A.K Gupta and M. Gupta, *Biomaterials*, 2004, **26**, 3995–4021.
- [35] S. Laurent, M. Mahmoudi, *Int J Mol Epidemiol Genet*, 2011, **2**, 367–90.
- [36] S. Laurent, D. Forge, M. Port, A. Roch, C. Robic, L.V. Elst, and R. N. Muller, *Chem Rev*, 2008,**108**, 2064–110.
- [37] W. Li, R. Liang, A. Hu, Z. Huang and Y. N. Zhou, *RSC Adv.*, 2014, **4**, 36959-966.
- [38] A. Fujishima and X. Zhang, *C R chimie*, 2005, **8**, 750–760.
- [39] F. Dilnawaz, A. Singh, C. Mohanty, S.K. Sahoo, *Biomaterials*, 2010, **31**, 3694–706.
- [40] L. Chen, F. Zang, H. Wu, J. Li, J. Xie, M. Ma, N. Gu and Y. Zhang, *Nanoscale*, 2018,**10**, 1788–1797.
- [41] Y. Nakamura, A. Mochida, P. L. Choyke, and H. Kobayashi, *Bioconjugate Chem*, 2016, **27**, 2225–2238.
- [42] J. Chomoucka, J. Drbohlavova, D. Huska, V. Adam, R. Kikez, J. Hubalek, *pharmacol. Res*, 2010, **62**,144–9.
- [43] S. Giri, B.G. Trewyn, M.P. Stellmaker, V.S.Y. Lin, *Angew Chem Int Ed Engl*. 2005, **44**, 5038- 44
- [44] S. Mura, J. Nicolas, P. Couvreur, *Nature Materials*, 2013, **12**, 991-1003.
- [45] Z. Sharafi, B. Bakhshi, J. Javidi, S. Adrangi, *Iranian J of pharmaceutical Research*, 2018, **17**, 386-395.
- [46] K. McNamara and S. A. M. Tofail, *Advances in Physics: X*, 2017, **2**, 54-88.
- [47] A.Kubacka, M. S. Diez, D. Rojo, R. Bargiela, S. Ciordia, I. Zapico, J. P. Albar, C. Barbas, *Scientific Reports*, 2014,**4**, 4134.

- [48] L. D. Matteis, R. F. Pacheco, L. Custardoy, M.L.G. Martin, *Langmuir*, 2014, 30, 5238.
- [49] Z. F. Yin, L. Wu, H. G. Yang and Y. H. Su, *Phys. Chem. Chem. Phys.*, 2013,**15**, 4844-4858.
- [50] W. Ren, L. Zeng, Z. Shen, L. Xiang, A. Gong, J. Zhang, C. Mao, A. Li, T. Paunesku, G. E. Woloschak, N. S. Hosmane and A. Wu, *RSC Adv.*, 2013,**3**, 20855-20861.
- [51] H. Deng, X. L. Li, Q. Peng, X. Wang, J. P. Chen and Y. D. Li, *Angew. Chem., Int. Ed.*, 2005, **44**, 2782-2785.
- [52] W. Li, J. Yang, Z. Wu, J. Wang, B. Li, S. Feng, Y. Deng, F. Zhang, and D. Zhao, *Journal of the American Chemical Society*, **2012**, **134**, 11864-867.[53] C. Wang, P. Li, J. Wang, Z. Rong, Y. Pang, J. Xu, P. Dong, R. Xiao and S. Wang, *Nanoscale* 2015, **7**, 18694-18707.
- [54] M.A. Habila, Z. A. ALOthman, A. M. El-Toni, J. P. Labis, M. Soylak, *Talanta*, 2016, **154**, 539-547.



Acknowledgements

I would like to express my sincere gratitude to my advisor Dr. Junghwan Oh, the professor of Department of Interdisciplinary program of Biomedical Mechanical & Electrical Engineering at Pukyong National University, for his valuable guidance and support throughout my master course. His great help, good advice, encouragement and all the other tremendous support during this research and thesis period is really an incredible experience for me.

I would like to thank my lab mates and friends for their timely support and help. I would like to convey my thanks to Dr. Santha, Dr. Sudip, Vy, Dr. Mani, Dr. Quang, Bian, Phuoc, Tu, Phong, Nam, Hye Hyun, Sumin, Dong hae and Jeayeop. Also, I am grateful to my husband, parents and my beloved for their unending love, support and encouragement during two year of master.

I take this opportunity to thank all those who have helped me directly or indirectly to complete this research work.

